NOVEL OPTICAL PROBES FOR BIOSENSING

A Dissertation

By

ANSAM JAMEEL TALIB

Submitted to the Office of Graduate and Professional Studies of
Texas A&M University
In partial fulfillment of the requirements for the degree of

DOCTOR OF PHILOSOPHY

Chair of Committee,	Alexei V. Sokolov
Co-Chair of Committee	Philip R. Hemmer
Committee Members,	Suhail Zubairy
	Olga Kocharovskaya
Head of Department,	Grigory Rogachev

May 2018

Major Subject: Applied Physics

ABSTRACT

Upconversion nanoparticles (UCNPs) are popular fluorescent probes for biological systems because of their immunity to autofluorescence background, photostability, and low toxicity. Nanodiamonds are also of interest for photostability and ultra-low toxicity. Finally, spectroscopic detection of certain dyes and Raman scattering spectroscopy also have biosensing applications. In this thesis, all approaches were investigated. In particular, upconversion nanoparticles with VO_4 were useful for sensing glucose without surface-functionalization and for reversibility. Applications of the technique for sensing glucose in persons with diabetes was proposed. Fabrication of UCNPs was optimized, and preliminary experiments initiated with red blood cell membranes and plants. Nanodiamonds and organic dyes were also used with red blood cell membranes. To optimize the use of our custom made nanoparticles in plants, we need to reduce their sizes while maintaining an appropriate level of brightness. This necessitated a tool that can measure brightness and size at the same time. For this, we built a custom confocal microscope and AFM combination.

DEDICATION

To my lovely:

Father and Mother

Brothers and Sisters

Husband, Mohanad

Children, Ali and Yousif

ACKNOWLEDGEMENTS

First, I would like to express my special thanks to my committee chair, Dr. Alexei V. Sokolov for his support, encouragement, supervision and mentoring. My sincere appreciation to my co-chair, Dr. Philip R. Hemmer for his guidance, kindness, support and everything else. Thanks also go to my committee members Dr. M. Suhail Zubairy and Dr. Olga Kocharovskaya for their time, support and challenging discussions of this research.

Many thanks to Dr. Bob Brick for his enthusiasm and support, and thanks to Ms. Sherree Kessler, Mr. Brendan Martin, Ms. RaéChel Superville, Dr. Emanuela Ene, Dr. Alexander Sinyukov, Dr. Carmen Gomes and Dr. Marlan O. Scully for all their help during my study.

I would like to thank my sponsor, the Higher Committee for Education Development in Iraq (HCED), and the Institute for Quantum Science and Engineering (IQSE), TAMU for their supports and funding.

I would like to thank all my friends during all my life, and also my friends and colleagues at Texas A&M University: Masfer H. Al-Kahtani, Yusef Maleki, Fahad Al-Ghannam, Abdulrahman Al-Methen, Linkun Jiang, Navid Rajil, Abdulrahman Alajlan, Sandra Lopez, Saeideh Shahrokh, Ruqayyah Asker, Eshtar Aluauee, and Aysenur Bicer.

My heartfelt thanks to my parents even though I know that there are no words adequately express my appreciation for them. Hopefully, this work was one way to say thanks. My father, you are always my superhero. My mother, thanks for your nurturing support; I am exceedingly saddned for losing you. When I worked on the diabetes project, you were always with me in my thoughts, and you will be in my heart and memories forever.

Thanks, also, to my brothers and sisters, other family members, and my mother-in-law, brothers-in-law and sisters-in-law for their endless support, encouragement and their valuable prayers.

My deepest thanks to my beloved husband Mohanad Yousif Hariz who brightens my life and always stands beside me and supports me with unfailing love. I could not have done this work without his support and patience throughout this entire process.

Finally, thanks to my sweethearts, Ali, and, Yousif. Thanks for being great boys. You are the light that guided me to finish this work whenever I felt frustrated, and life gave me challenges. I just try to remember your words that you said together one day "Mom, we are proud of you" and now it is my turn to say that I am proud of both of you.

.

CONTRIBUTORS AND FUNDING SOURCES

This work was supported by a dissertation committee consisting of Dr. Alexei V. Sokolov (advisor), Dr. Philip R. Hemmer (co-advisor), Dr. M. Suhail Zubairy and Dr. Olga Kocharovskaya.

This graduate study was supported by a sponsorship from Iraq through the Higher Committee for Education Development in Iraq (HCED) program. We also acknowledge support from the National Science Foundation (grant# CHE1609608), the Office of Naval Research (grant# N00014-16-1-2578), and the Welch Foundation (grant # A- 1547).

NOMENCLATURE

UCNPs	Upconversion nanoparticles
UC	Upconversion
ETU	Energy transfer upconversion
NP	Nanoparticles
VO_4	Vanadium oxide
ND	Nanodiamond
NV	Nitrogen vacancy color centers
SiV	Silicon vacancy color centers
RBCs	Red blood cells
RBCMs	Red blood cell membranes
Hb	Hemoglobin
R6G	Rhodamine 6G
AFM	Atomic Force Microscope
Pt/Ir	Platinum-Iridium
NIR	Near infra-red
DLS	Dynamic light scattering
TEM	Transmission electron microscope
Re^{+3}	Valence state of rare earth elements, in general
PVA	Poly vinyl alcohol

TABLE OF CONTENTS

Page

LIST OF FIGURES

Page

LIST OF TABLES

Page

CHAPTER I

INTRODUCTION TO BIOSENSORS FOR GLUCOSE MONITORING

Diabetes (Hyperglycemia) endangers the health of millions of people all over the world. According to the International Diabetes Federation (IDF) in 2015, there are 415 million people worldwide living with Diabetes. In 2017, IDF reported one of two adults with diabetes is undiagnosted, there are 425 million adults have diabetes. This number is expected to increase to 649 million in 2045. Diabetes has become a worldwide chronic disease problem.

Diabetes is a long-lasting disease caused by the inability of the pancreas to produce sufficient insulin (Type 1 Diabetes) or the body is not able to make good use of the insulin it produces (Type 2 Diabetes). For non-diabetic people, whenever they experience high blood sugar, the pancreas promotes insulin release. This insulin stimulates glucose removal from the blood by allowing it to cross cell membranes. After this the glucose can 1) be converted to ATP, 2) be converted to fat, and 3) short-term storage of the glucose by conversion to glycogen in the liver and muscle tissue. In all cases, it will lower the blood sugar level. Conversely, when there is low blood sugar, the pancreas releases a hormone glucagon that promotes glucose release from cells and raises blood sugar.

During a day, the glucose level in blood of a human body varies depending on eating or fasting conditions, but it should be kept between 70-120 mg/dl as a reasonable level. If the glucose level in the blood of someone bellows 70 mg/dl, he or she will suffer from hypoglycemia. Hypoglycemia can cause a feeling of tiredness, lethargic, coma and in the severe situation can lead to death. Hyperglycemia is when the glucose level goes above 120

mg/ dl. Then, there is a risk of having severe health problems such as blindness, kidney failure, stroke, nerve issues [1, 2].

There is no cure for diabetes at this time. Therefore, people with diabetes need to take their medication regularly by injection of insulin (type 1 diabetes) or taking pills (type 2 diabetes) to maintain blood glucose (BG) level in the acceptable range and prevent diabetes complications. To determine the correct dosage of insulin, continuous monitoring of blood glucose levels is essential. Therefore a sequence of appropriate glucose biosensors has been developed [3, 4].

In general, biosensors can be branded into different sets: optical, electrochemical, thermometric, piezoelectric or magnetic depending on the method of signal transduction. The most common kind of biosensors is optical. Optical biosensors are excellent substitutes for analytical techniques because they have high specificity, sensitivity, small size, cost-effectiveness, and for many biological and chemical substances they have real-time and label-free detection [5, 6].

In the last decades, there has been exponential growth in the research and technology to develop optical biosensors. There are many applications of biosensors in the fields of medicine, the environment, and biotechnology. For example, the handheld glucose meter used by diabetics is one of the most commercially successful applications of a biosensor. Unfortunately, these meters are inconvenient for patients because they require needle sticking to collect blood samples [7-9]. Pricking a finger is painful. These meters work based on indirect electrochemical detection of hydrogen peroxide produced by enzymatic oxidation of glucose which generates an electrical current. The current is carried by a cable

to a portable monitor that analyzes and displays the glucose level in blood [7]. Moreover, even though this glucose meter is cheap, it has a sensor strip that is expensive.

There are many other generations of glucose sensors, but they all have limitations: some are very expensive, affordable ones are not reliable or accurate, and most cause patient complaints. For example, these include minimally invasive methods such as using smart contact lens by Google. However, these bring discomfort to the user. Current noninvasive glucose-meters like the smartwatch by Dexcom is considered costly to maintain and need calibration every 12 hours. Also, since diabetes has become worldwide chronic disease problem, better, affordable sensors are needed.

To overcome the limitations of existing glucose sensors, direct, low-cost, and non-invasive optical glucose sensors are proposed. For example, some optical sensors are based on the change in emission intensity and fluorescence-lifetime as a function of glucose concentrations [10]. These include organic dyes, quantum dots (QDs), and noble metal nanoparticles (NPs) functionalized with a boronic acid, which provides sensitive and reversible glucose level monitoring systems [11-16]. However, most optical sensors are limited by photostability, especially for dyes, and toxicity, especially for dyes and QDs. Also, noble metal nanoparticles are sensitive to other factors in the local environment where their emission can be affected by pH level [17-20].

To offset these drawbacks, lanthanide-ion-(rare earth elements)-doped nanocrystals, especially those that function as upconversion nanoparticles (UCNPs) have recently been investigated. UCNPs operate based on energy transfer upconversion (ETU) in which sensitizer ion (typically ytterbium, Yb^{+3}) absorbs near infrared (NIR) laser (mostly 980 nm

laser). Due to its broad NIR absorption cross-section, and sequentially transfers absorbed energy to the upconverting ions such as (Er^{+3}, Ho^{+3}, and Tm^{+3}) [21-23]. Consequently, the upconverting ions emit visible to NIR emission, where the autofluorescence background of the biological tissues is significantly suppressed. Figure 1 shows the energy transfer via a metastable level in Er^{+3}.

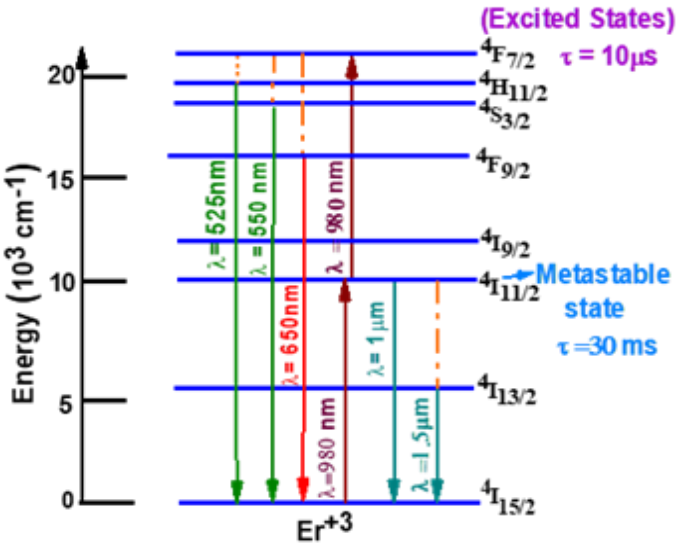

Figure 1: Energy transfer levels in Er^{+3}.

Nevertheless, there are mainly two issues that might limit the use of the UCNPs as an optical glucose sensor. First, to make UCNPs sensitive to glucose, they must be functionalized, for example, with manganese dioxide (MnO_2)-nanosheets [24] or molecules like boronic-acid. However, these can be affected by bloodstream conditions, such as pH level resulting in reduced measurement sensitivity and reversibility. Second, the maximum absorption of the typical sensitizer of UCNPs (Yb^{+3}) overlaps with the strong absorption of water at 980 nm and can cause heating [25, 26]. This can also interfere with glucose sensing because UCNPs respond to temperature changes as well [27-32].

CHAPTER II

SYNTHESIS AND CHARACTERIZATION OF UPCONVERSION NANOPARTICLES

2.1 INTRODUCTION

Here, we report the use of water-tolerant upconversion nanoparticles YVO_4 and $GdVO_4$: Er, Yb@Nd in a core/shell structure with no any surface functionalization for accurate and reversible optical glucose sensing. The advantage of core/shell UCNPs is that they can be efficiently excited at a wavelength (808 nm) where heating due to water absorption is minimized.

In this work, we chose yttrium vanadium oxide (YVO_4) as host crystals because of the reported interaction of the vanadium oxide ion with glucose [33-35] and gadolinium vanadium oxide ($GdVO_4$) because they can be made very small. In addition, YVO_4 and $GdVO_4$ crystals have shown high upconversion efficiency and good photostability in water as reported in [30, 36-38]. However, in the future, Gd toxicity considerations may necessitate the use of only YVO_4 crystals. For this study, we prepared two nanoparticles: first, $YVO_4:Yb^{+3},Er^{+3}@Nd^{+3}$ core/shell UCNPs with an average size of 20 nm with silica gel during the treatment, which was discussed in detail in [31]. Next, we prepared $GdVO_4:Yb^{+3},Er^{+3}@Nd^{+3}$ UCNPs in core/shell structure, with average size 60-80nm, without silica gel during the annealing time [30].

2.2 MATERIALS FOR SYNTHESIS

The following chemicals were used in the experiment as received: D- Glucose ($C_6H_{12}O_6$) [MACRON FINE CHEMICALS], D- Fructose($C_6H_{12}O_6$) [Alfa Aesar], Poly vinyl alcohol (PVA) [Sigma-Aldrich], Sodium orthvanadate Na_3VO_4 [Sigma- Aldrich], 99.9 % gadolinium(III) nitrate hexahydrate, $Gd(NO_3)_3$:$6H_2O$ [99.9%, Sigma- Aldrich], erbium(III) nitrate pentahydrate, $Er(NO_3)_3$:$5H_2O$ [99.9%, Sigma- Aldrich], ytterbium(III) nitrate pentahydrate,$Yb(NO_3)_3$:$5H_2O$ (99.9%, Sigma- Aldrich), Neodymium(III) nitrate hexahydrate $Nd(NO_3)_3$: $6H_2O$ [99.9% Sigma- Aldrich]. Sodium citrate [Sigma- Aldrich], Yttrium (III) nitrate Y (NO_3) [99.9% Sigma- Aldrich]. Phenylboronic acid (99%) (Alfa-Aesar). The fluorescence spectra were achieved with our custom-built confocal microscope. Transmission electronic image (TEM) images were obtained using JEM- 2010 Electron Microscope.

2.3 SYNTHESIS UCNPS $(Y/Gd)VO_4:Yb^{+3},Er^{+3}$ CORE/ SHELL

Briefly, for both nanoparticles, $(Y/Gd)VO_4:Yb^{+3},Er^{+3}$ core nanoparticles were prepared following a hydrothermal synthesis procedure previously described in [37-39].

2.3.1 CORE SYNTHESIS

A 10 ml solution of $Y(NO_3)_3.4H_2O$ (87% mol/L) or $Gd(NO_3)_3.4H_2O$ (87% mol/L)], plus $Er(NO_3)_3.5H_2O$ (2% mol/L), and $Yb(NO_3)_3.5H_2O$ (2% mol/L) was prepared and slowly added dropwise using a peristaltic pump to a 7.5 ml solution of sodium citrate (0.1 mol/L). These rare earth (Re^{+3})-sodium citrate mixtures were kept under vigorous stirring until a white participate was formed. Then, a second solution consisting of 10 ml of sodium orthovanadate Na_3VO_4 (0.1 mol/L) dissolved in distilled water was added slowly to the

(Re^{+3}-sodium citrate) mixture under constant stirring with a few drops of 1 M NaOH to maintain the pH above 11 for an hour at room temperature to form $(Y/Gd)VO_4:Yb^{+3},Er^{+3}$ core nanoparticles.

For the synthesis of core-only particles, the mixture was transferred into a polytetrafluoroethylene (PTFE) vessel (as shown in Figure 2a). The vessel was placed in a stainless steel high-pressure autoclave chamber (as shown in Figure 2b) and kept under 7 MPa pressure, and 230 ^oC for 24 h. Then, the $(Y/Gd)VO_4:Yb^{+3},Er^{+3}$ core nanoparticles were collected after washing three times with pure water and centrifugation (10,000 rpm for 10 min).

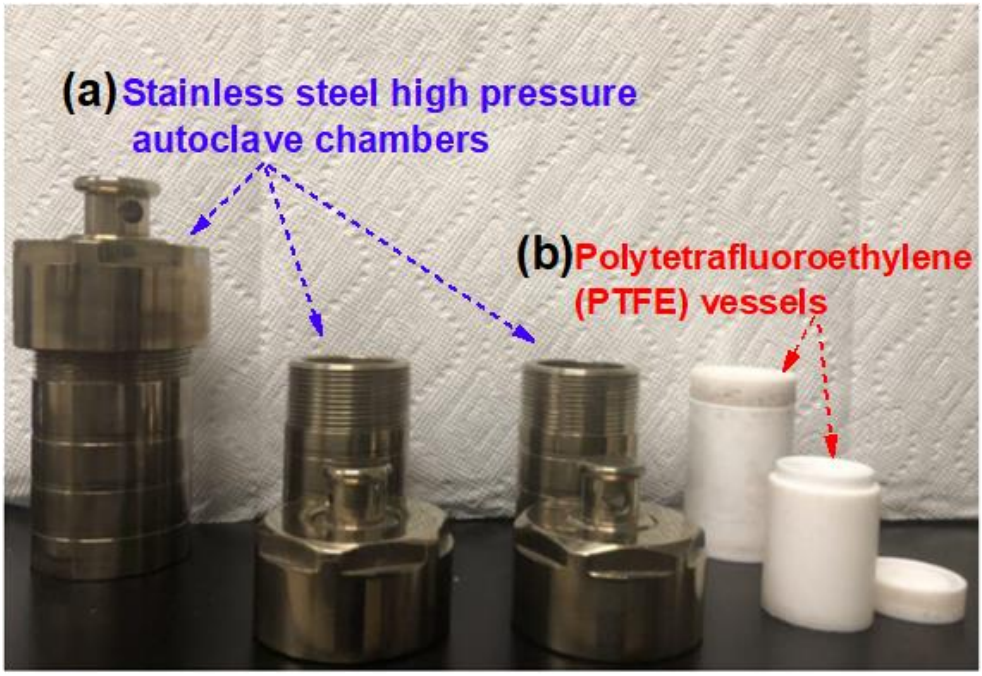

Figure 2: (a) polytetrafluoroethylene (PTFE) vessels. (b) Stainless steel, high- pressure autoclave chambers.

2.3.2 PREPARING SHELL MIXTURE

A 10 ml solution of $(\mathrm{Y\ or\ Gd})\mathrm{NO_3)_3.4H_2O}$ (87% mol/L, plus $\mathrm{Nd(NO_3)_3.5H_2O}$ (2% mol/L), and $\mathrm{Yb(NO_3)_3.5H_2O}$ (2% mol/L) was prepared and slowly added dropwise to a 7.5 ml solution of sodium citrate (0.1 mol/L) using a peristaltic pump. This rare earth (Re^{+3})-sodium citrate mixture was kept under vigorous stirring until a white participate was formed. Then a second solution consisting of 10 ml of sodium orthovanadate Na_3VO_4 (0.1 mol/L) dissolved in distilled water was added slowly to (Re^{+3}-sodium citrate) mixture under constant stirring with a few drops of 1 M NaOH to maintain the pH above 11 for 1 hour at room temperature to form the shell solution.

2.3.3 CORE/ SHELL SYNTHESIS

For Core/Shell structure synthesis, Nd^{+3} was introduced to $(\mathrm{Y/Gd})\mathrm{VO_4}:\mathrm{Yb^{+3}},\mathrm{Er^{+3}}$ core nanoparticles by overgrowing a shell layer (3-4 nm) of $(\mathrm{Y/Gd})\mathrm{VO_4}:\mathrm{Yb^{+3}},\mathrm{Nd^{+3}}$ at ($\mathrm{Yb^{+3}}$ 10%, $\mathrm{Nd^{+3}}$10%) doping ratio. We approach that by mixing the core mixture (as described in core synthesis above) and shell mixture (described above) as follows: the shell nanoparticles mixture was added slowly dropwise to the core nanoparticles mixture and kept under constant stirring for an hour. Next, the final mixture was transferred into an autoclave for hydrothermal treatment at 230 ^{o}C for 24 hours. After that, it was left to cool until reaching the room temperature. The concentrations of $\mathrm{Yb^{+3}}$ and $\mathrm{Nd^{+3}}$ in the shell layer were carefully optimized, as reported in [26]. Finally, the YVO_4: Yb^{+3}, Er^{+3}@$Nd^{+3,}$ and $GdVO_4$: Yb^{+3}, Er^{+3}@Nd^{+3} core/shell nanoparticles were obtained.

2.4 TEM IMAGES OF THE UCNPS NANOPARTICLES (YVO_4: Yb^{+3}, Er^{+3}@Nd^{+3}, AND $GdVO_4$: Yb^{+3}, Er^{+3}@Nd^{+3})

We performed transmission electron microscope (TEM) imaging for YVO_4: Yb^{+3}, Er^{+3}@Nd^{+3}, and $GdVO_4$: Yb^{+3}, Er^{+3}@Nd^{+3} nanoparticles. For TEM and optical characterization of $GdVO_4$: Yb^{+3}, Er^{+3}@Nd^{+3} UCNPs, a droplet was placed on a carbon grid for TEM imaging. Figure 3 (a and b) shows low and high magnification TEM images that reveal dispersed and well-crystallized nanoparticles with average size (60-80 nm) as shown in Figure 3 (c), which were expected to exhibit a strong upconversion luminescence. The unexpected expansion in size is due to high temperature treatment at 1000C for 10 mins without using silica-gel. Silica-gel has been reported to maintain the desired size during high temperature annealing [37-39]. The TEM image of YVO_4: Yb^{+3}, Er^{+3}@Nd^{+3} showed the particle sizes to be around 20 nm as shown in Figure 3 (d).

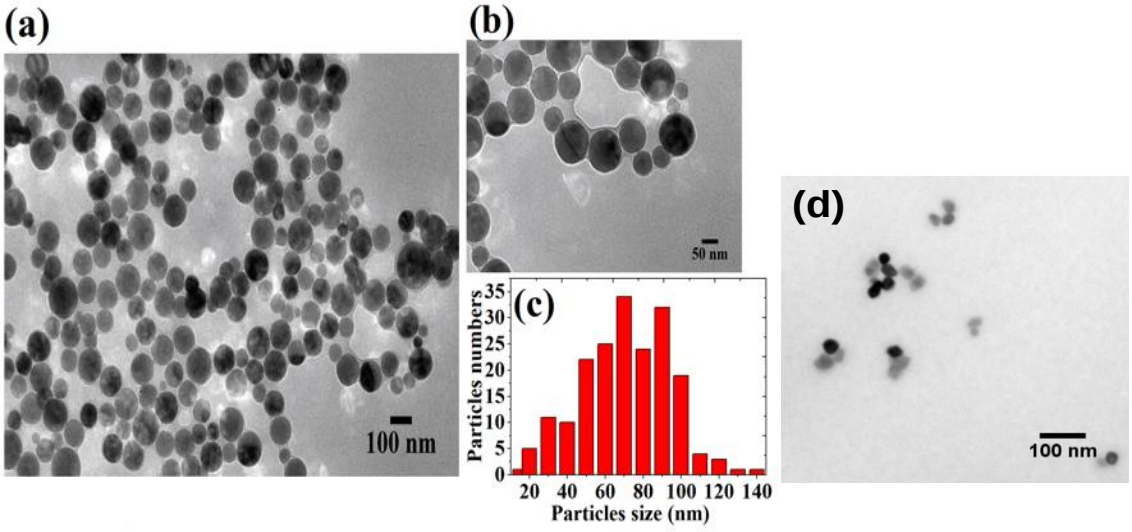

Figure 3: TEM images of (a, b) $GdVO_4$: Yb^{+3}, Er^{+3}@Nd^{+3}, (c) size particles of $GdVO_4$: Yb, Er^{+3}@Nd^{+3} and (d) YVO_4: Yb^{+3}, Er^{+3}@Nd^{+3} nanoparticles.

2.5 OPTICAL CHARACTERIZATION OF UCNPS

For optical characterization of YVO_4 and $GdVO_4$: Yb^{+3}, Er^{+3}@Nd^{+3} core/shell UCNPs, a custom confocal laser scanning microscope setup was built, as shown in Figure 4. The optical confocal microscope is equipped with a 90x, NIR microscope objective with NA=0.8, and 808 nm laser diode for optical excitation. After filtering, the excitation laser with a short-pass (750 nm SP) filter, the upconversion fluorescence of the UCNPs was collected through the same microscope objective and analyzed with a homemade spectrometer equipped with a starlight camera (Trius camera model SX-674), and a photon counter (Hamamatsu photon counter model number H7155-21).

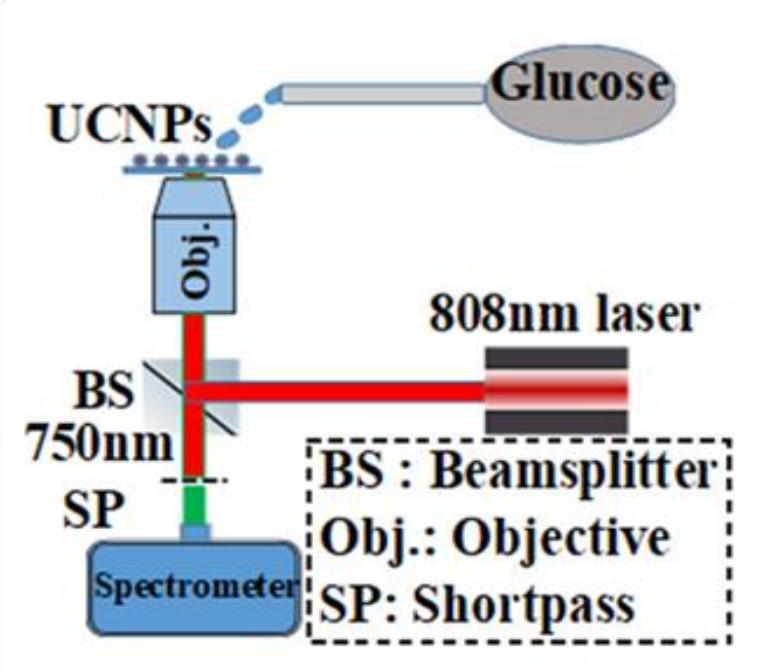

Figure 4: An illustration of a custom- built confocal microscope equipped with visible–near infrared objective, NIR laser, and visible laser.

As stated above both YVO_4 and $GdVO_4$: Yb^{+3}, Er^{+3}@Nd^{+3} core/shell UCNPs function based on upconversion energy transfer as reported in [31]. As shown in figure 5(a), a near-infrared (NIR) photon (808 nm) excites Nd^{+3} to its $^4F_{5/2}$ excited state, followed by non-radiative relaxation to $^4F_{3/2}$ state. The energy transfer populates $^2F_{5/2}$ state of nearby Yb^{+3} in the shell, and then crosses the shell layer towards nearby Yb^{+3} in the core to populate its $^2F_{5/2}$ state to initiate the typical UC process in the Er^{+3} ion. In the core, the energy transfer from the $^2F_{5/2}$ excited state of Yb^{+3} promotes Er^{+3} to its $^4I_{11/2}$ metastable state. Sequentially, a second NIR photon's energy transfer from the $^2F_{5/2}$ excited state of Yb^{+3} further excites the Er^{+3} to highly excited ($^2H_{11/2}$, $^4S_{3/2}$, and $^4F_{9/2}$) Er^{+3} states via the multi-phonon transfers. Consequently, two strong green emissions and one weak red emission occur, corresponding to these transitions: $^2H_{11/2}\rightarrow{}^4I_{15/2}$, $^4S_{3/2}\rightarrow{}^4I_{15/2}$, and $^4F_{9/2}\rightarrow{}^4I_{15/2}$, respectively.

To verify the operation of these upconversion particles, a thin layer of $GdVO_4$: Yb^{+3}, Er^{+3}@ Nd^{+3} core/shell UCNPs was uniformly distributed on a glass microscopic cover slide. Figure 5(b) illustrates a clear upconversion spectrum of $GdVO_4$: Yb^{+3}, Er^{+3}@Nd^{+3} core/shell UCNPs at a relatively low laser intensity of 800 mW/cm^2. The optical spectrum shows upconversion peaks located at (525 nm, 552.8 nm, and 650 nm) corresponding to $^2H_{11/2}\rightarrow{}^4I_{15/2}$, $^4S_{3/2}\rightarrow{}^4I_{15/2}$, and $^4F_{9/2}\rightarrow{}^4I_{15/2}$ transitions of the Er^{+3} ion.

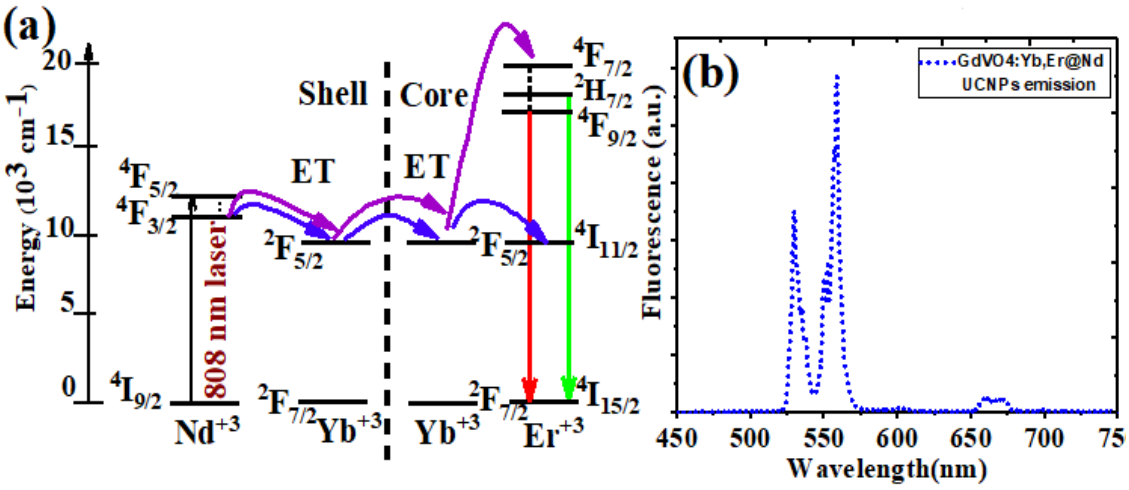

Figure 5: (a)Upconversion energy transfer of $YVO_4:Er^{+3},Yb^{+3}$@ Nd^{+3} and $GdVO_4:Er^{+3},Yb^{+3}$@ Nd^{+3}, (b) Fluorescence spectrum of $GdVO_4:Er^{+3},Yb^{+3}$@ Nd^{+3} excited with laser 808 nm.

2.6 CONCLUSION

In conclusion, we synthesized small YVO_4 and $GdVO_4$: Yb^{+3}, Er^{+3}@Nd^{+3} UCNPs in a core/shell structure where their excitation wavelength was in a biocompatible band. YVO4: Yb^{+3}, Er^{+3}@Nd^{+3} UCNPs were treated with silica gel during the annealing process to maintain their original sizes. Silica-gel has been reported to maintain the desired size during high temperature annealing. While $GdVO_4$: Yb^{+3}, Er^{+3}@Nd^{+3} UCNPs were not treated with silica gel during the annealing process, and that explains the increasing in their sizes is due to high temperature treatment at 1000C for 10 mins without using silica-gel.

CHAPTER III

GLUCOSE SENSING PROCEDURES WITH UCNPS

3.1 UCNPS IN AQUATIC SOLUTIONS

3.1.1 BORONIC ACID FUNCTIONALIZED UCNPS

Boronic acid has been used as a sensor for glucose. Boronic acid modified fluorescent UCNPs of YVO_4: Yb^{+3}, Er^{+3}@Nd^{+3} was fabricated and investigated by following the same procedure as described in [40]. Briefly, 0.2 g of phenylboronic acid was dissolved in 20 mL of DI water, then 0.02 g of UCNPs was added to the above solution. The final solution was sonicated for 10 min, followed by adjusting the pH to 9.0 by adding 0.1 M NaOH under constant stirring. To remove dissolved O_2, the solution was bubbled with nitrogen gas for an hour while being stirred. The final solution was transferred into a polytetrafluoroethylene (PTFE) vessel. The vessel was placed into a stainless steel high-pressure autoclave chamber, and the temperature adjusted to 160 ^{o}C for 8 hours. After cooling to room temperature, the UCNPs containing solution was centrifuged at 10,000 rpm for 30 min, and the pellet was resuspended with DI water. To further purify the functionalized UCNPs, the resultant solution was dialyzed in a dialysis bag for 24 hours to remove any unwanted chemical and to wash the nanoparticles with DI water. The purified functionalized UCNPs were preserved at 4 °C for further use.

After functionalization, the particles core/shell UCNPs were buffered by combining 150 μL of 0.1 M PBS buffer solution (pH = 7.4) with 20 μL of an aquatic solution of YVO_4: Yb^{+3}, Er^{+3}@ Nd^{+3}. This solution was then placed into a 2mL colorimetric tube. Many more

identical tubes were then prepared in the same way. Then, different amounts of glucose were added to each tube. The mixtures in each tube were then diluted to a volume of 1 mL by adding water and mixing thoroughly. After one hour, a tiny droplet of each sample with different glucose concentrations was placed onto a microscope coverslip, and allowed to dry in the air for 10-15 minutes. Later, the fluorescence spectra of each sample was recorded by operating our custom built confocal microscope (using laser 532 for excitation and 550 nm long pass filter), as shown in Figure 6.

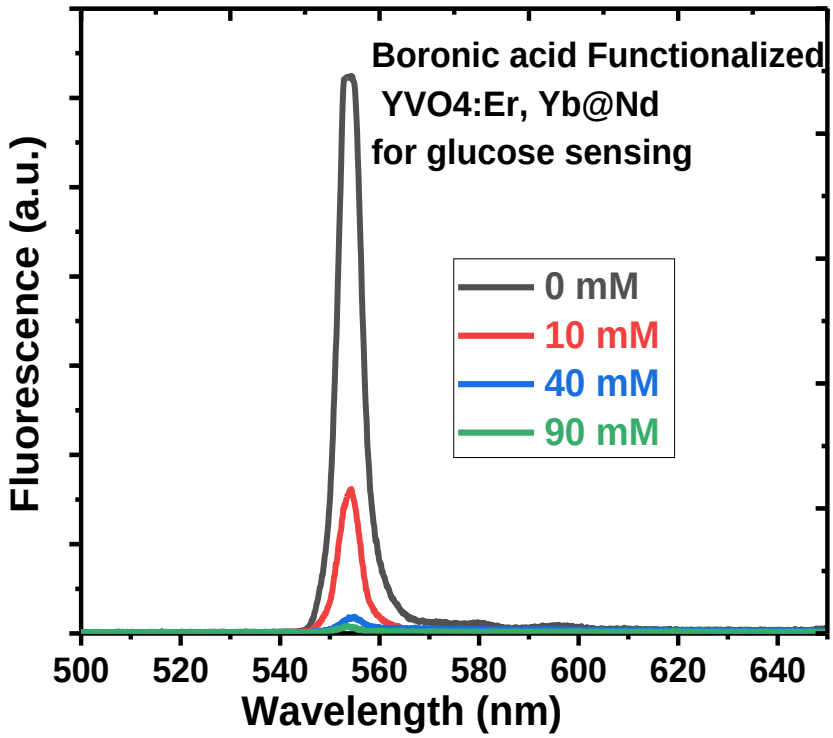

Figure 6: Fluorescence spectra of boronic- acid- functionalized UCNPs (YVO_4: Er^{+3}, Yb^{+3}: Nd^{+3}) with different concentrations of glucose excited with laser 532nm.

3.1.2 BARE PARTICLES

As a control experiment, the above experiment was repeated with bare particles without the boronic acid for two different concentrations of glucose, and the data is shown in Figure 7.

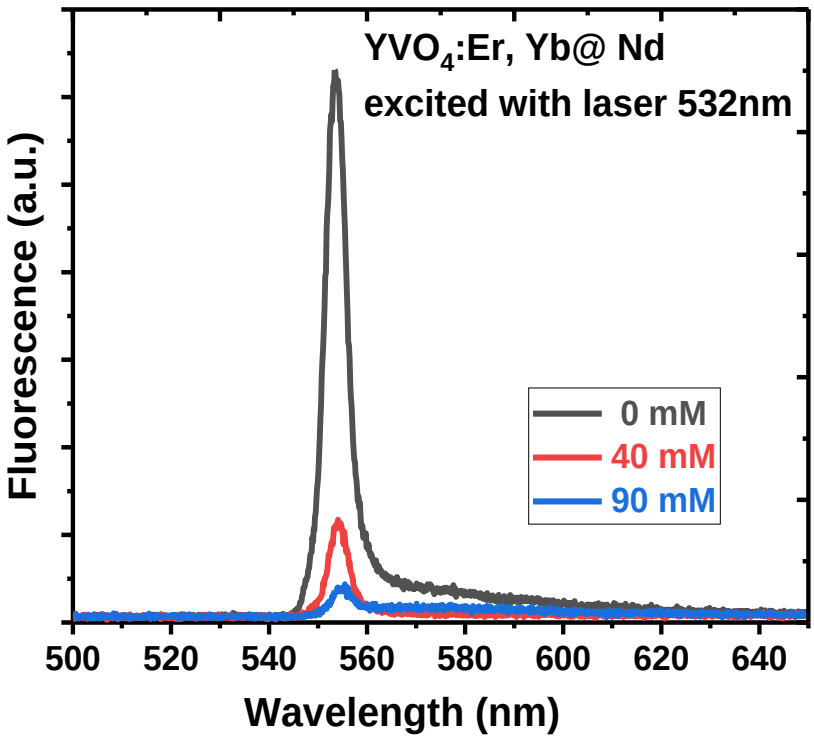

Figure 7: Fluorescence spectra of UCNPs (YVO_4: Er^{+3}, Yb^{+3}: Nd^{+3}) with different concentration of glucose, excited with laser 532nm.

The spectra showed that the florescence intensities were quenched by increasing glucose concentrations. The results for bare UCNPs are very similar to the boronic acid modified UCNPs, discussed above. To confirm these results, we repeated the experiment using many more glucose concentrations (0 mM, 1 mM, 100 mM and 1000 mM). We also

excited with an 808 nm laser instead of the 532 nm laser. The resulting fluorescence spectra were recorded by using our custom built confocal setup and are shown in Figure 8.

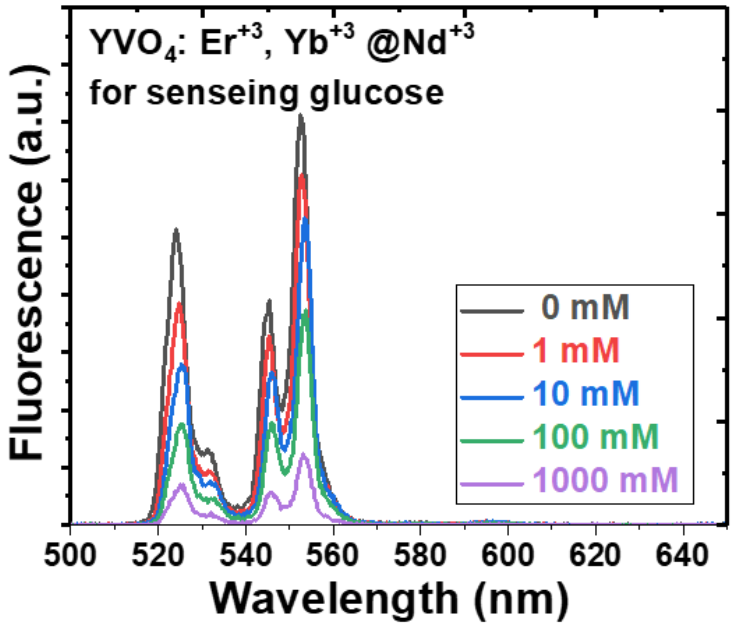

Figure 8: Upconversion luminescence spectra of YVO_4: Yb^{+3}, Er^{+3}@Nd^{+3} core/shell UCNPs recorded as a function of different glucose concentrations (0-1000 mM). UC luminescence of YVO_4: Yb^{+3}, Er^{+3}@Nd^{+3} core/shell UCNPs decreased gradually with increasing glucose concentrations from 0 to 1000 mM.

The fluorescence spectra showed glucose sensitivity over a wide range of concentrations starting from very low to very high. Again, these UCNPs YVO_4: Yb^{+3}, Er^{+3}@Nd^{+3} were able to sense the glucose without any functionalization. These results were encouraging and led to more measurements to be described next.

3.2 FIXING THE UCNPS' IN PVA FOR FUTURE REVERSIBLE SENSING DEMONSTRATION

To demonstrate reversible optical glucose sensing of the particles without boronic acid, a layer of dispersed UCNPs was fixed to a microscope slide, so that the same particles could be investigated while the glucose concentration was changed. To fix the UCNPs, 20 μL each of YVO_4: Yb^{+3}, Er^{+3}@$Nd^{+3,}$ and also $GdVO_4$: Yb^{+3}, Er^{+3}@Nd^{+3} core/shell upconversion nanoparticles were mixed with a polyvinyl alcohol (PVA): water solution (1:1) and spin-coated on separate microscope coverslips. Then, the two spin-coated microscope slides (Y and Gd) were covered with an additional microscope coverslip to create a flow-channel to allow changing of glucose concentration and afterward to return to the original concentration to verify reversibility, as illustrated in Figure 9.

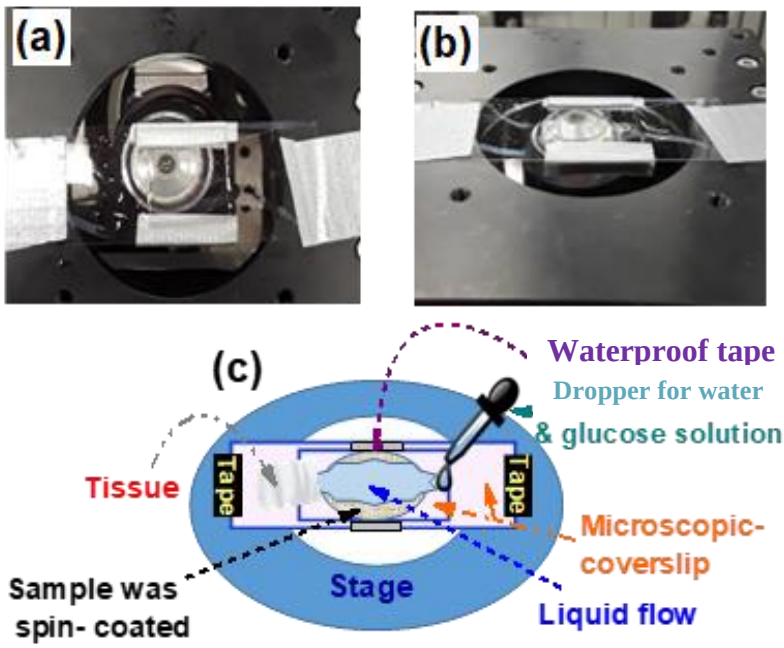

Figure 9: The experimental setup of rinsing technique: (a) top view picture of the technique, (b) side view picture, and (c) schematic of the rinsing technique.

Using the experimental procedure outlined in Figure 9, the optical glucose sensing results are shown in figure 10(a) for YVO_4: Yb^{+3}, Er^{+3}@Nd^{+3} core/shell UCNPs sample (average size 20 nm). As seen, the upconversion (UC) luminescence of YVO_4: Yb^{+3}, Er^{+3}@Nd^{+3} core/shell UCNPs decreased gradually with increasing glucose concentrations from 0 to 30 mM. The influence of the glucose concentration on the quenching efficiency of the 552.8 nm emission line is summarized by the plot in Figure 10 (b).

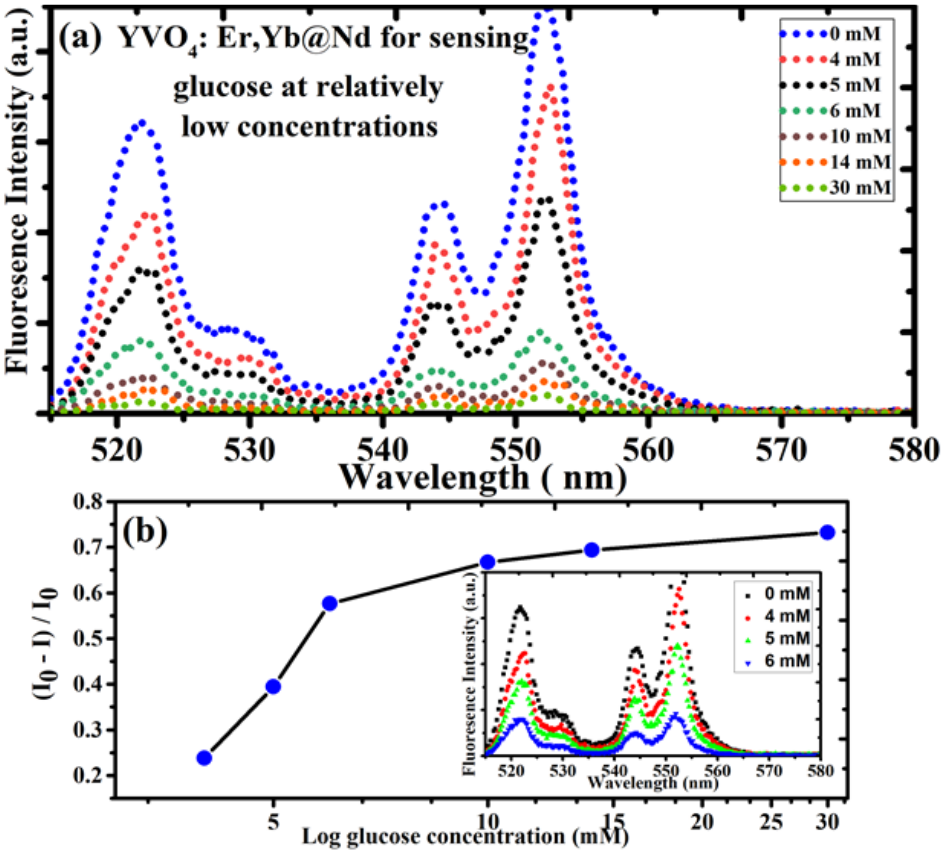

Figure 10: (a) Upconversion luminescence spectra of YVO_4: Yb^{+3}, Er^{+3}@ Nd^{+3} core/shell UCNPs recorded as a function of different glucose concentrations (0-30 mM).(b) Influence of glucose concentrations on quenching efficiency at 552.8 nm. (b, inset) Change of YVO_4: Yb^{+3}, Er^{+3}@Nd^{+3} core/shell UCNPs emission spectra over normal blood glucose range (4-6 mM).

Here, the quenching efficiency was defined as $(I_0\text{-}I)/I_0$, where I_0 and I represent the fluorescence intensity without and with glucose; respectively, at the 552.8 nm line of YVO_4: Yb^{+3}, Er^{+3}@ Nd^{+3}.

At first, the quenching increased linearly with the glucose concentration, throughout the range of reasonable glucose level in human blood (from 4 to 6 mM) and then saturates at around 70% beyond 10 mM. Figure 10 (b, inset) shows the UC spectra quenching as a function of glucose concentrations in the range of normal blood (0 to 6 mM). Table 1 shows the glucose concentrations in mM corresponding to blood glucose level in mg/dl units that covers the standard monitoring range for blood glucose in humans and also shows the health risk corresponding to each glucose level.

Table 1: Mean glucose level (fasting).

Glucose concentration (mM)	Blood glucose level (mg/dl)	Risk
1	18	Very High
2	36	Very High
3	54	High
4	72	No risk
5	90	No risk
6	106	No risk
7	126	medium
8	195	Medium
9	162	Medium
10	180	Medium
11	196	Medium
12	216	High
15	270	High
20	360	Very high
30	540	Very high
40	720	Very high
50	900	Very high

Next, optical glucose sensing using $GdVO_4$: Yb^{+3}, Er^{+3}@Nd^{+3} core/shell UCNPs (average size 20 nm) was investigated using the same procedure as before. For these, Figure 11 (a and b) again shows a strong quenching of the UC luminescence with increasing glucose concentrations. The quenching efficiency for high glucose concentrations at 552.8 nm was calculated and plotted in Figure 11 (c). Again, the quenching efficiency was defined as $(I_0-I)/I_0$, where I_0 and I represent the fluorescence intensity without and with glucose, respectively; at the 552.8 nm line of $GdVO_4$: Yb^{+3}, Er^{+3}@ Nd^{+3}. As can be seen the response to glucose is similar to the YVO_4 particles.

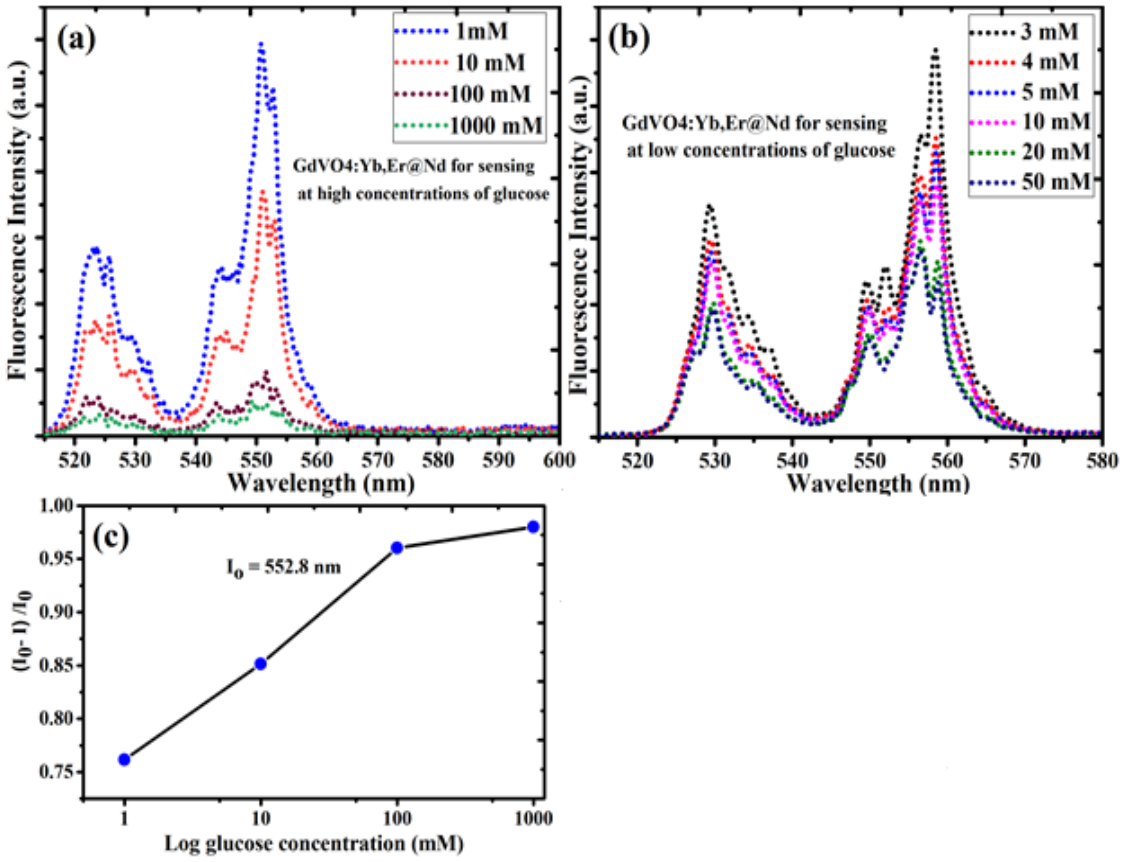

Figure 11: (a and b) Upconversion luminescence spectra of $GdVO_4$: Yb^{+3}, Er^{+3}@Nd^{+3} core/shell UCNPs recorded as a function of high and low glucose concentrations. (c) Influence of the glucose concentrations on the quenching efficiency at 552.8 nm.

3.3 IMMUNITY OF GLUCOSE SENSING TO LASER INTENSITY AND PARTICLE SIZE FLUCTUATIONS VIA RELATIVE INTENSITIES

To demonstrate the possibility of accurately sensing glucose in the presence of laser intensity fluctuations, we performed a normalized plot of the UC spectra quenching as a function of glucose concentrations, as illustrated in Figure 12. Here, the UC spectra are normalized to the maximum peak at 552 nm. As it can be seen, the ratio of emission peaks heights also senses glucose, and hence, it is possible to develop a sensor that is immune to intensity fluctuations caused by the laser or some other interferent.

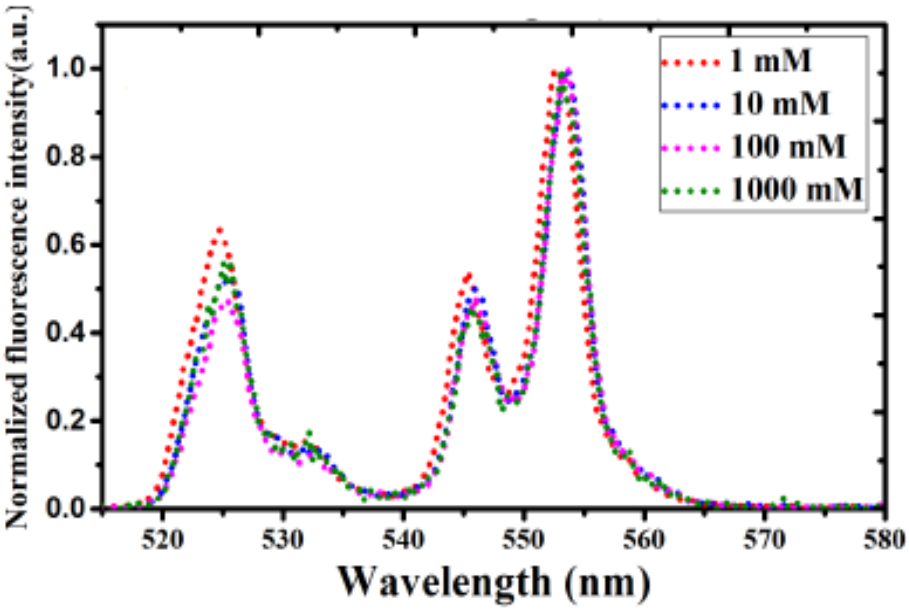

Figure 12: Normalized upconversion spectra of YVO_4: Yb^{+3}, Er^{+3}@Nd^{+3} core/shell UCNPs as a function of high glucose concentrations.

3.4 THE REVERSIBILITY OF OPTICAL GLUCOSE SENSING

To verify that glucose sensing is reversible, we flowed different concentrations of glucose over the particles, then flowed DI water over the particles to remove the glucose. Figure 13 shows the reversible quenching of UC luminescence of $GdVO_4$: Yb^{+3}, Er^{+3}@Nd^{+3} core/shell UCNPs. First, the spectrum was measured without glucose, then 50 mM glucose was flowed over the particles, and the spectrum measured again. As seen the glucose produced quenching. Then DI water was flowed over the particles to rinse away the glucose, and the fluorescence intensity was recovered as shown in Figure 13 (a).

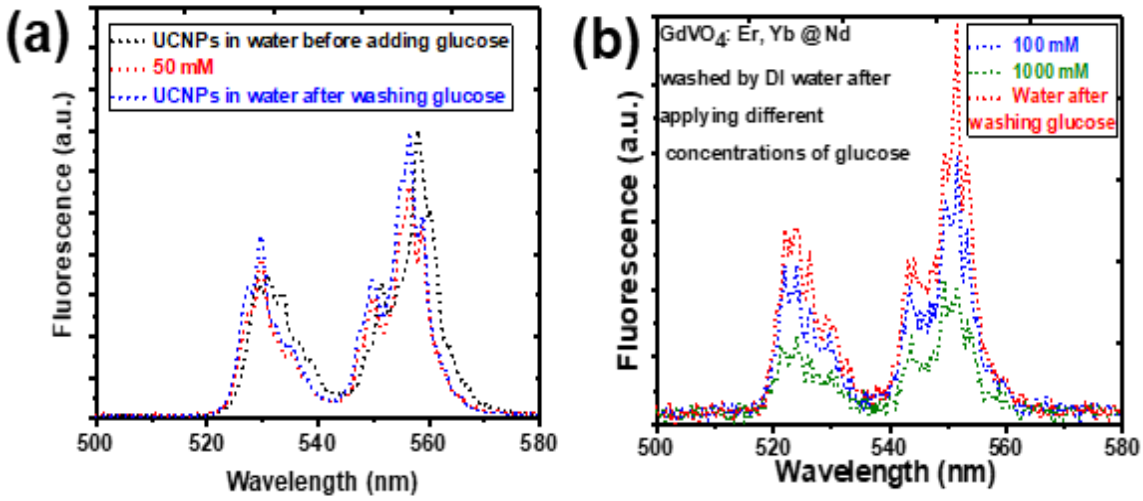

Figure 13: The reversible quenching of UC luminescence of $GdVO_4$: Yb^{+3}, Er^{+3}@Nd^{+3} core/shell UCNPs. (a) (50 mM) and (b) (1 mM, 10 mM, 100 mM, and 1000 mM) glucose was added in different concentrations to produce quenching, then the fluorescence intensity was recovered after rinsing with DI water.

The experiment was then repeated on another sample. First, the spectrum of pure water was measured. Then different concentrations of glucose (0 mM, 1 mM, 10 mM, 100 mM and 1000 mM) were applied to produce florescence quenching, and finally, the fluorescence intensity was again recovered after rinsing with DI water. However, for high glucose concentrations the recovery was not complete as shown in Figure 13 (b) (i.e. the fluorescence level did not return completely to the initial pure water case but was somewhat lower). This is possibly related to our inability to thoroughly rinse the nanoparticles with our crude setup. Nonetheless, the fluorescence intensity after rinsing away the 1000 mM glucose was still higher than that seen for the 100 mM concentration.

3.5 SENSING FRUCTOSE

It is important to investigate the specificity of $GdVO_4$: Yb^{+3}, Er^{+3}@Nd^{+3} core/shell UCNPs fluorescence quenching to glucose to estimate the performance in the presence of interferents. To do this, we repeated the experiment at the same concentrations as before, but this time with glucose replaced by fructose. As shown in Figure 14, we observed no quenching effect of fructose on the UC luminescence of the UCNPs. This indicates that $GdVO_4$: Yb^{+3}, Er^{+3}@Nd^{+3} core/shell UCNPs are sensitive and selective for glucose (at least compared to fructose).

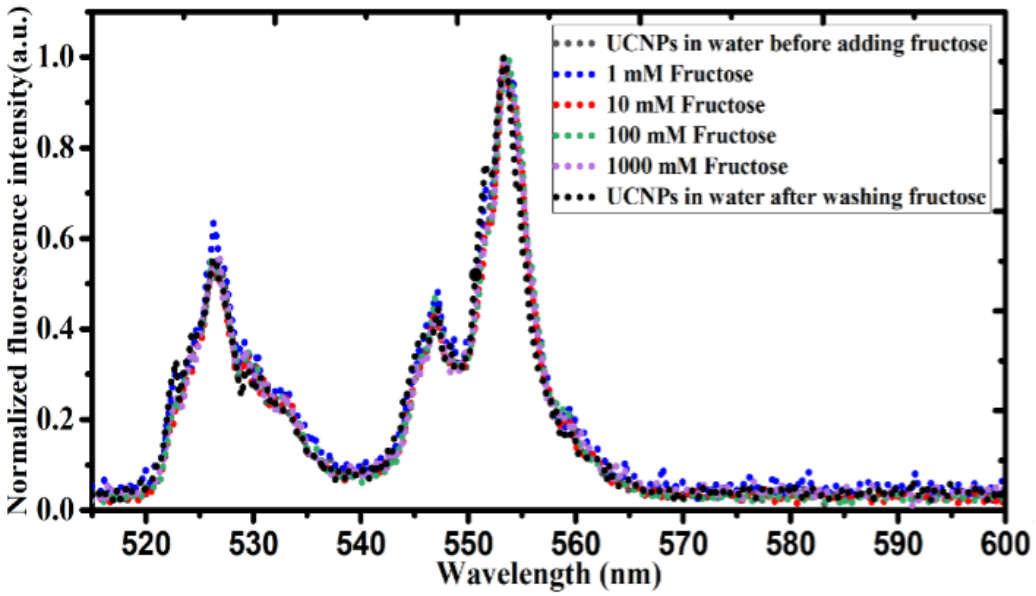

Figure 14: Unchanged upconversion spectra of $GdVO_4$: Yb^{+3}, Er^{+3}@Nd^{+3} core/shell UCNPs after adding and washing fructose concentrations.

3.6 CONCLUSION

In conclusion, we showed that these UCNPs are sensitive, reversible and selective glucose sensors, without the need for functionalization or surface modifications that might cause toxicity or shelf-life issues. This feature makes YVO_4 and $GdVO_4$: Yb^{+3}, Er^{+3}@Nd^{+3} upconversion nanoparticles especially interesting for glucose sensing in biological systems such as monitoring the blood glucose level in humans.

CHAPTER IV

SENSING GLUCOSE IN PLANTS

4.1 INTRODUCTION

The world population may exceed 9.7 billion people by the year 2050 [41] More reliable crop yields will be needed within the coming decades to ensure that enough food is available in the future. Many plant breeding efforts seek to overcome fluctuations in crop yields due to stress like drought, heat, climate changes [42]etc. [43] To do this, better techniques are needed to measure plant stress *in vivo* in real time. The idea is to develop noninvasive or minimally invasive technologies for stress detection that give real-time results in the field environment. That would allow a farmer to intervene early [44]. For this we need to monitor large numbers of different plants and different parameters related to plant productivity. Nowadays, several factors limit *in vivo* sensing technologies such as the time obligatory for detecting a stress response, the level of stress and its type, and/or physiological changes [45].

Also rapid screening of new plant phenotypes are needed to develop advanced stress-resistant crops. For this, physiological, biochemical, and morphological characteristics of plants should be monitored. Here, the key is to accurately predict plant growth and biomass (crop) production, in the presence of known or unknown stresses before any visible signs appear on the plant.

Plant growth requires light energy, carbon dioxide, water, and minerals. Abiotic stress is produced by environmental circumstances like heat, drought, soil salinity, ect. These

can decrease growth and crop yield [46]. The key is finding the best monitor to detect the future effects of such stress long before crop failure occurs.

During photosynthesis, the plant's leaf will use the carbon dioxide (CO_2) and water (H_2O) in the presence of sunlight or other source of light energy and chlorophyll to produce glucose ($C_6H_{12}O_6$) and oxygen (O_2) in an endothermic reaction. In addition to producing glucose, plants are a vital source of oxygen on the earth. Glucose is used by the plant for respiration (for energy), making complex carbohydrates (cellulose and starch), making amino acids (with nitrates) as proteins, and making oils and fats. Therefore, the relation of glucose production to eventual crop yield is simple; if there is no glucose production, there will be no crops.

$$6CO_2 + 6\,H_2O \xrightarrow[\text{Chlorophyl}]{\text{Light energy}} C_6H_{12}O_6 + 6O_2$$

There are several possible sources of abiotic stress which may impact the process of photosynthesis and plant growth. These include ultraviolet (UV) light [47-49], unseasonable droughts, low or high temperature of the environment [46, 49], and soil salinity [46, 50]. In general plants show a dynamic and sophisticated response to abiotic stress [51]. This

response can be described as elastic (reversible) or plastic (irreversible) [46]. However, lacks needed precission in the absence of more precise knowledge. Figure 15 shows a simulation for glucose level versus time and how glucose level might vary depending on the different source of stresses.

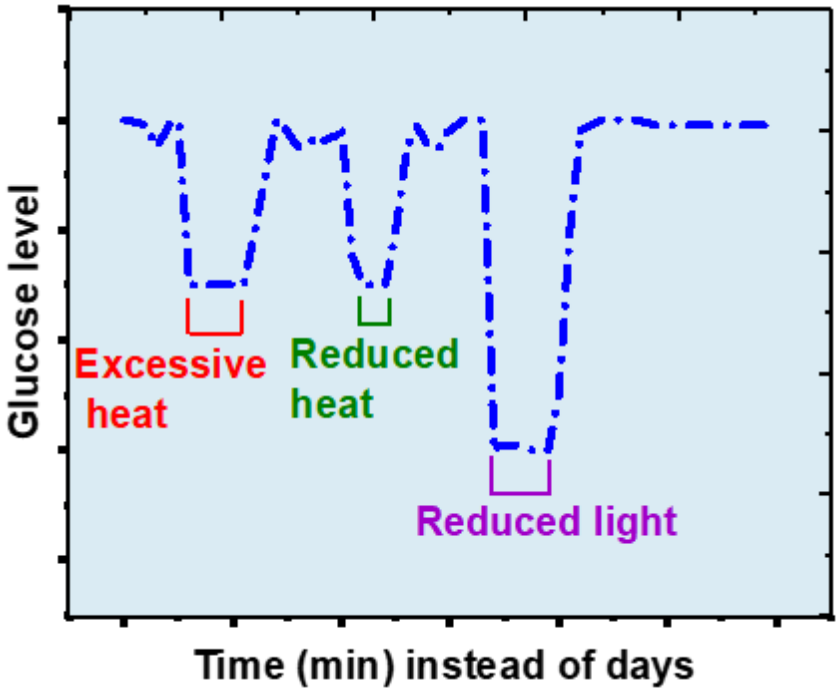

Figure 15: A simulation shows how glucose levels can vary depending on the different source of stress.

Therefore, measuring glucose production may be a way of rapidly measuring stress in plants. During photosynthesis, plant manufactures glucose in the leaves. Surplus glucose is soon converted into starch, which is stored. Currently, there are three methods commonly

used to measure the level of glucose in leaves: Fehling's, Tollen's and Benedict's solutions. These detect the aldehyde group in glucose.

Here, we propose an experiment to find a noninvasive and rapid technique to deterimine glucose levels in real-time and if this is a reliable indication of plant stress that will affect crop yields. For this work, we propose the use of rare earth upconversion nanoparticles (UCNPs) that can sense glucose.

Recently, UCNPs have attracted attention for biomedical and bioimaging applications [50, 52-54]. These nanoparticles have unique luminescent properties, for instance, superior photostability, the ability to convert low energy near infrared (NIR) photons to higher energy photons usually in visible light, sharp emission lines, and no autofluorescence [55-57].

Two techniques can be used to facilitate absorption of nanoparticles by plants. First, through the foliar entry which can happen through the cuticle, via stomata, and wounds. Another technique that has been used is root entry. The nanoparticles can be taken through root tips, lateral roots, root hairs, and ruptures.

Several researchers recently have studied UCNPs in plants. Their focus was on the effects of size and shape of UCNPs in plants [58-60]. The small size of nanoparticles enables them to selectively go to certain parts of the plants. For example, smaller nanoparticles can go to the leaf faster after being uptaken by the roots. In addition, surprising research, done by Juanjuan Peng, and *et al.*, [61], shows that plant growth can be promoted by feeding them with UCNPs.

4.2 MATERIALS AND METHODS

The following compounds were acquired from Sigma- Aldrich Co.: Sodium orthovanadate Na_3VO_4 (99.9%), gadolinium(III) nitrate hexahydrate, $Gd(NO_3)_3{:}\,6H_2O$ (99.9%), erbium(III) nitrate pentahydrate, $Er(NO_3)_3{:}\,5H_2O$ 99.9%, , ytterbium(III) nitrate pentahydrate, $Yb(NO_3)3{:}\,5H_2O$ (99.9%), Neodymium(III) nitrate hexahydrate $Nd(NO_3)3{:}\,6H_2O$ (99.9%). Sodium citrate, Yttrium(III) nitrate $Y(NO_3){:}\,4\,H_2O$ (99.9%). Plant food (Miracle-Grow) was obtained from a local vendor.

Fluorescence spectra were collected with our custom-built confocal microscope and spectrometer. The fluorescence images were obtained using a Zeiss LSM 780 NLO Multiphoton Microscope. TEM images were obtained with a JEM-2010 Electron Microscope.

4.3 SYNTHESIS: (Y or Gd)$VO_4{:}\,Er^{+3}, Yb^{+3}$AND $GdVO_4{:}\,Eu^{+3}, Yb^{+3}$ CORE UCNPS

Briefly, for each type of nanoparticle $(Y/Gd)VO_4{:}\,Yb^{+3}, Er^{+3}$and $GdVO_4{:}\,Eu^{+3}$, Yb^{+3} core nanoparticles were prepared following a hydrothermal synthesis procedure previously described in [37-39].

4.3.1 CORE SYNTHESIS

A 10 ml solution of $Y(NO_3)_3.\,4H_2O$ (87% mol/L) or $Gd(NO_3)_3.\,4H_2O$ (87% mol/L), plus (Er or Eu)$(NO_3)_3.\,5H_2O$ (2% mol/L), and $Yb(NO_3)_3.\,5H_2O$ (2% mol/L) was prepared and slowly added dropwise using a peristaltic pump to a 7.5 ml solution of sodium citrate (0.1 mol/L). These rare earth (Re^{+3})-sodium citrate mixture was kept under vigorous stirring

until a white participate was formed. Then, a second solution consisting of 10 ml of sodium orthovanadate Na_3VO_4 (0.1 mol/L) dissolved in distilled water was added slowly to (Re^{+3}-sodium citrate) mixture under constant stirring with a few drops of 1 M NaOH to maintain the pH above 11 for 1 hour at room temperature. For the synthesis of core-only particles, the mixture was transferred into a polytetrafluoroethylene (PTFE) vessel. The vessel was placed into a stainless steel high-pressure autoclave chamber and kept under 7 MPa pressure, and 230°C for 24 hours. Then, the $(Y \text{ or } Gd)VO_4: Yb^{+3}, Er^{+3}$ and $GdVO_4: Yb^{+3}, Eu^{+3}$core nanoparticles were collected after washing three times with pure water and centrifugation (10000 rpm for 10 min).

4.3.2 PREPARING SHELL MIXTURE FOR YVO_4 AND $GdVO_4$ CORE/ SHELL

A 10 ml solution of $(Y \text{ or } Gd)NO_3)_3.4H_2O$ (87% mol/L, plus $Nd(NO_3)_3.5H_2O$ (2% mol/L), and $Yb(NO_3)_3.5H_2O$ (2% mol/L) was prepared and slowly added dropwise to a 7.5 ml solution of sodium citrate (0.1 mol/L) using a peristaltic pump. This rare earth (Re^{+3})-sodium citrate mixture was kept under vigorous stirring until a white participate was formed. Then a second solution consisting of 10 ml of sodium orthovanadate Na_3VO_4 (0.1 mol/L) dissolved in distilled water was added slowly to (Re^{+3}-sodium citrate) mixture under constant stirring with a few drops of 1 M NaOH to maintain the pH above 11 for 1 hour at room temperature to form the shell solution.

4.3.3 SYNTHESIS CORE/ SHELL UCNPS: $YVO_4: Er^{+3}, Yb^{+3}@\ Nd^{+3}$ AND $GdVO_4: Eu^{+3}, Yb^{+3}@\ Nd^{+3}$

For core/shell structure synthesis, Nd^{+3} was introduced to $YVO_4: Yb^{+3}, Er^{+3}$ *and* $GdVO_4: Yb^{+3}, Eu^{+3}$ core nanoparticles by overgrowing a shell layer (3-4 nm) of $YVO_4: Yb^{+3}, Nd^{+3}$ *and* $GdVO_4: Yb^{+3}, Nd^{+3}$ at (Yb^{+3} 10%, Nd^{+3}10%) doping ratio. We approach that by mixing the core mixture (as described in core synthesis above) and shell mixture (described above) as following: the shell nanoparticles mixture was added slowly dropwise to the core nanoparticles mixture and kept under constant stirring for an hour. Next, the final mixture was transferred into an autoclave for hydrothermal treatment at 230 ^{o}C for 24 hours. After that, it was left to cool until reaching room temperature. The concentrations of Yb^{+3} and Nd^{+3} in the shell layer were carefully optimized, as reported in [26]. Finally, the YVO_4: Yb^{+3}, Er^{+3}@$Nd^{+3,}$ and $GdVO_4$: Yb^{+3}, Eu^{+3}@Nd^{+3} core/shell nanoparticles were obtained.

4.4 TEM IMAGES

TEM measurements will be an essential way to find out the size of UCNPS. We performed transmission electron microscope (TEM) imaging for $YVO_4: Yb^{+3}, Er^{+3}@Nd^{+3}$, $GdVO_4: Yb^{+3}, Eu^{+3}@Nd^{+3}$, and $GdVO_4: Er^{+3}, Yb^{+3}$ nanoparticles. The TEM samples were prepared by dropping each solution onto a carbon grid. The TEM image of $GdVO_4: Yb^{+3}, Er^{+3}$ show small UCNPs with average sizes (5 nm) as shown in Figure 16 (a). $YVO_4: Yb^{+3}, Er^{+3}@Nd^{+3}$ shows an average size as 20 nm as shown in Figure 16 (b).

The TEM image $GdVO_4: Eu^{+3}, Yb^{+3}$ @Nd^{+3} shows very small UCNPs with average size (5-8 nm) as shown in Figure 16 (c).

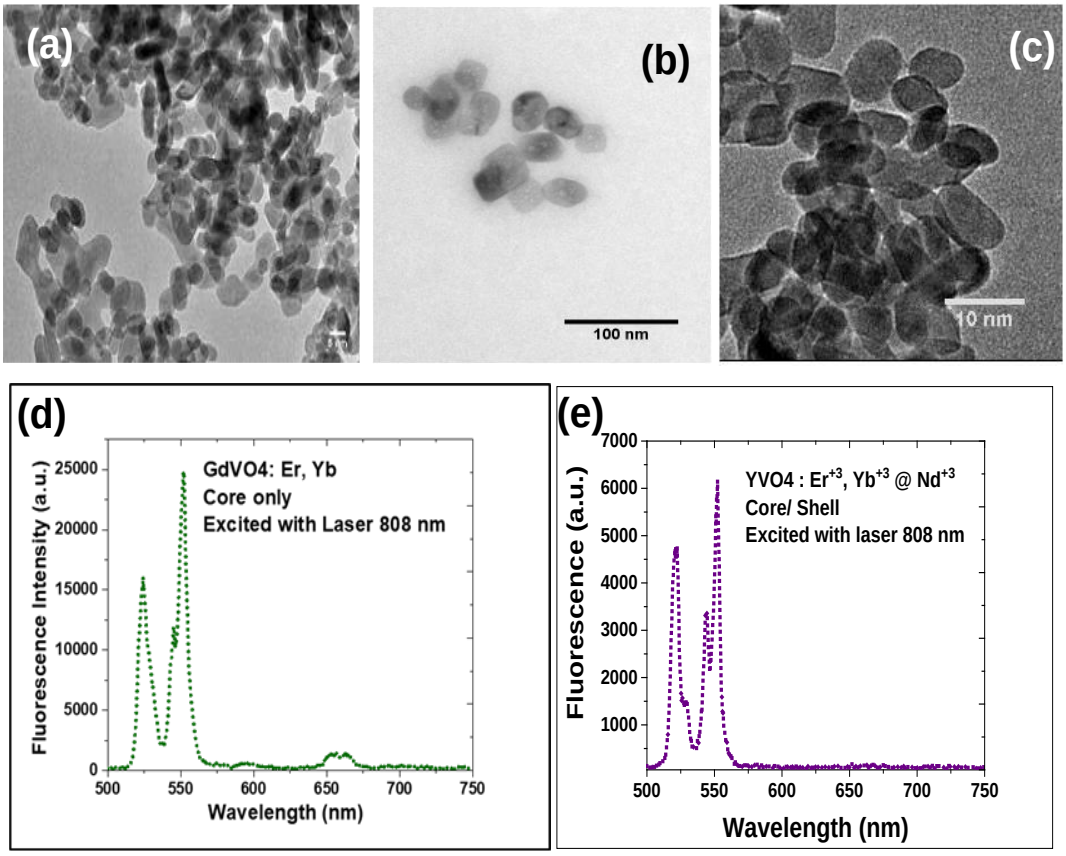

Figure 16: TEM images of UCNPs: (a) $GdVO_4$: Er^{+3}, Yb^{+3} core NPs. (b) YVO_4: Er^{+3}, Yb $^{+3}$@Nd^{+3} core/shell. (c) $GdVO_4$: Eu^{+3}, Yb^{+3} @ Nd^{+3} core /shell.

4.5 EXPERIMENTAL

4.5.1 PUMPKIN SEEDLINGS FED WITH UCNPS.

In this study, we choose pumpkin seedlings as a model. In the beginning, the seeds were planted in soil. After four days (when the seedlings started growing and had two seed leaves), the plants were transferred from the soil, and the roots of the seedlings were washed with fresh water several times. Next, the pumpkin seedlings were reared in a hydroponic system as shown in Figure 17 (a). Later, two seedlings were removed and placed into a glass jar containing UCNPs in solution as shown in Figure 17 (b). Figure 17 (c) shows TEM image of the UCNPs ($YVO_4 : Er, Yb$ @ Nd) with average size ~20 nm which was used to feed the plants. The UCNP solution was made by dissolving 62.5 mg of UCNPs in 50 ml of water. Then, the mixture was sonicated for 15 minutes to separate any clumps of nanoparticles. Later, 200 ml of water was added to above mixture to dilute, and the pH was adjusted to 6. We observed a healthy growth for these two pumpkin seedlings, where one is shown in Figure 17 (d).

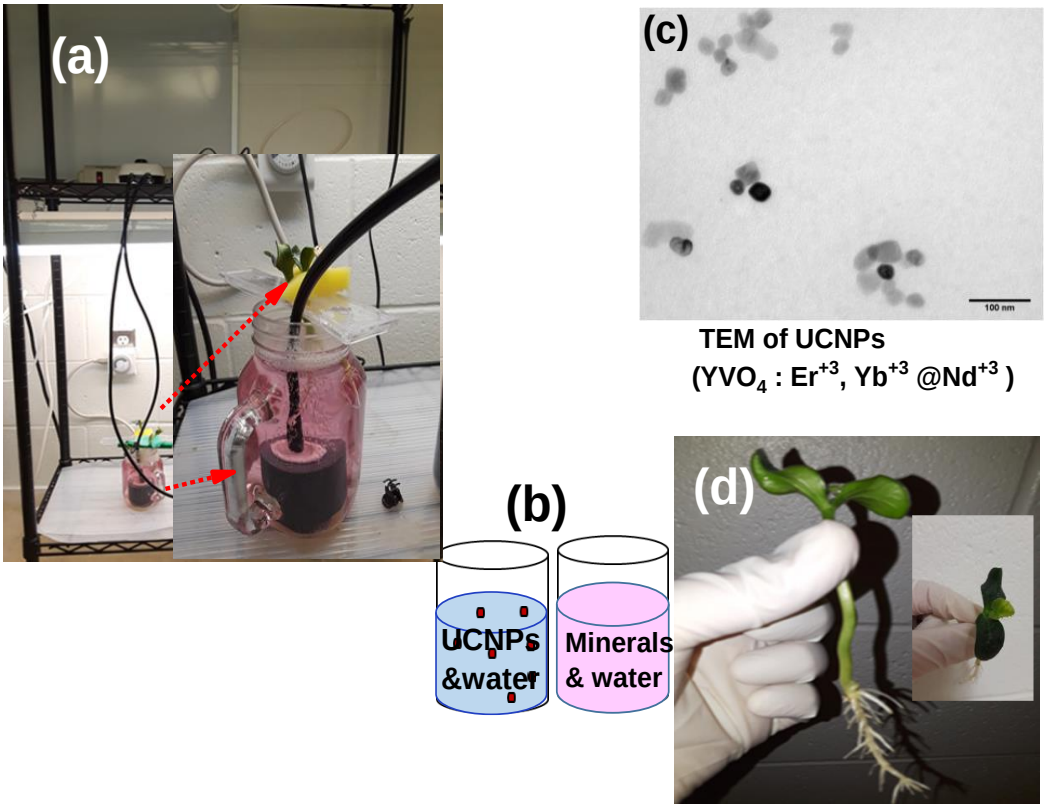

Figure 17: Pumpkin seedlings fed with UCNPs (a) Hydroponic method to grow plants. (b) The left (blue) water and UCNPs mixed together and right water and plant food (pink). (c) TEM image of the UCNPs $\mathbf{YVO_4}$: $\mathbf{Er^{+3}}$, $\mathbf{Yb^{+3}@Nd^{+3}}$. (d) real photo to the pumpkin seedling fed with UCNPs.

Before measuring the pumpkin seedlings fed with UCNPs, we looked at a seed leaf injected with UCNPs. The injected leaf was washed several times to ensure there was no UCNPs outside the leaf. The leaf was placed between microscope coverslips. Tape was applied from two sides to keep the leaf flat.

The confocal fluorescence microscope was used to collect optical and fluorescence images from different spots of the leaf as in Figure 18.

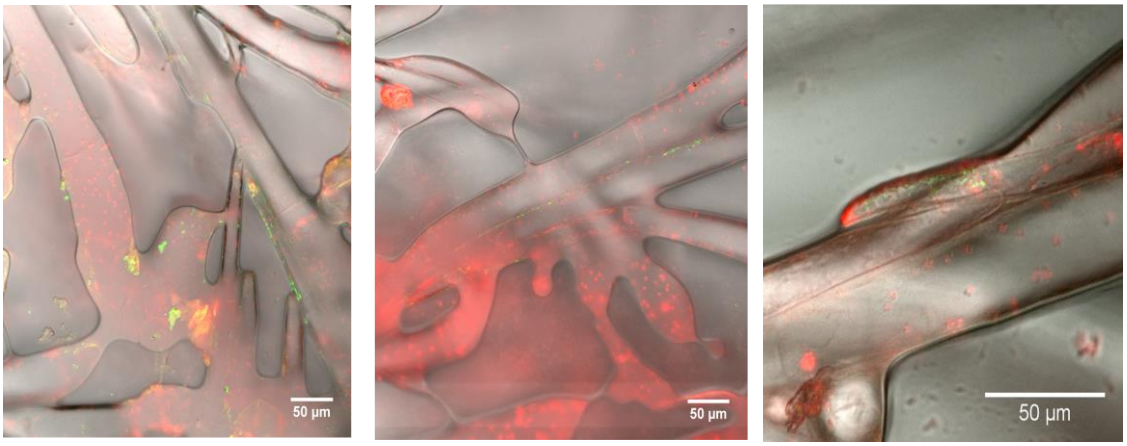

Figure 18: Optical and fluorescence images combined together from different spots of injected leaf which were excited with lasers 808 nm excitation (green) and 561nm(red).

Next, fluorescence spectra were measured for a second seed leaf that was injected with core-only UCNPs. These spectra were obtained by using our custom-built confocal microscope with 532 nm and 808 nm laser excitations, as in Figure 19. As seen, the 532 nm spectrum is dominated by background biofluorescence.

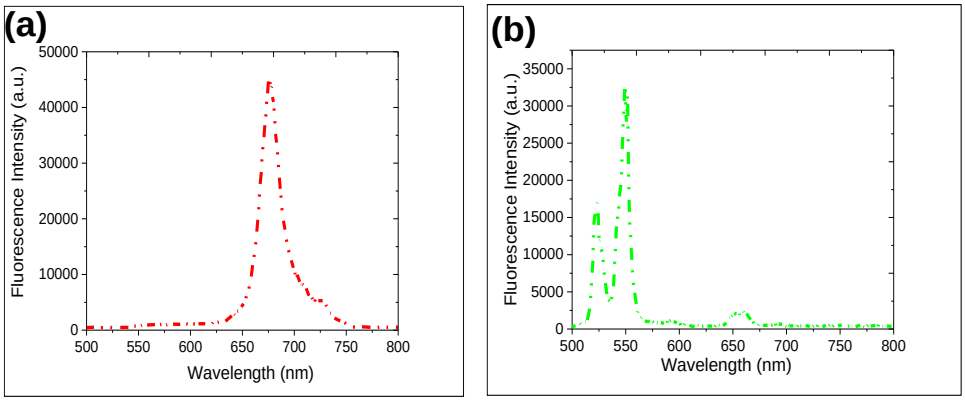

Figure 19: Fluorescence spectra from different spots from the injected leaf with UCNPs
(a) Fluorescence spectrum from pumpkin seedling's seed leaf excited with laser 532nm.
(b) Fluorescence spectrum from pumpkin seedling's seed leaf excited with laser 808nm.

Later, the plants that were watered with UCNPs were studied using 808 nm excitation as shown in F igure 20. The pumpkin seedling was cut to study leaf, stem, and root, separately. A clean blade was used to cut each part to avoid any cross contamination. The leaf, upper stem, and roots from the pumpkin seedlings fed with UCNPs were washed with fresh water several times, then each one was placed between microscope coverslips. Tape was applied to both sides to secure the specmens as in Figure 20 (a).

The commercial confocal fluorescence microscope was used to collect optical and fluorescence images from these samples. For the leaf a 40-X objective was used and the laser excitation was 808 nm, while the emission was collected between (500-600 nm) as in Figure 20 (b). The upper stem was excited with both 808 nm and 561 nm lasers and the images were combined with a white light image in Figure 20 (c). Again, considerable autofluorescence (red dots) was seen when the sample was excited with the 561 nm laser. There was no autofluorescence when excited with the 808 nm laser. The root, images were taken with lasers at 808 nm and 561nm plus optical images are shown in Figure 20 (d).

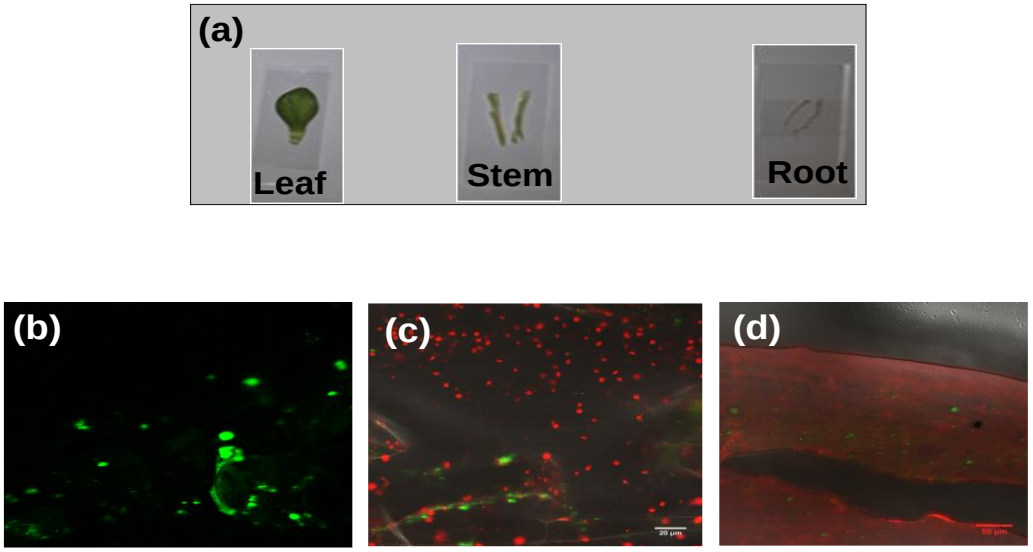

Figure 20: Images of plants (pumpkin seedlings) fed, not injected, with UCNPs: (a) the plant was cut to small parts such as leaf, stem and root, and these pieces were placed between two microscope coverslips. Tape was used to stick the two coverslips together. (b) Fluorescence image of UCNP fed –seed "leaf" – using 40X objective and laser 808 nm for excitation and fluorescence produced by emission is collected within the 500-600 nm range. (c) Combined bright field image and laser excitation at 808 nm and 561 nm image of UCNPs fed- Upper Stem- 40X objective. (d) Combined bright field image and lasers excitation at 808 nm (green) and 561nm (red) for root from the pumpkin seedling fed UCNPs- 20X objective.

4.5.2 SENSING GLUCOSE AND/OR OXYGEN IN PLANTS

As discussed above, to sense the glucose levels in plants during photosynthesis we propose feeding the plants with UCNPs that can be absorbed by the root and transported to

the leaves in a short time depending on the nanoparticles sizes. In this way, UCNPs can be a simple and rapid method to detect glucose *in vivo.*

Another way to detect photosynthesis would be by sensing the oxygen produced. Sensing oxygen can be done with the nitrogen-vacancy NV center in diamond as was observed by S. Steinert and *et al.*, [62] In this way, we can use two techniques for sensing photosynthesis for confirming each measurement.

For this experiment, we plan to use *Egeria densa* as a model (Brazilian waterweed a large-flowered waterweed) as a model (Figure 21).

Figure 21: *Egeria densa* in a small aquarium.

Egeria densa has often been used to study photosynthesis [63] because the oxygen can be observed as bubbles even with low light excitation. This makes *E. densa* an excellent candidate to sense both glucose and oxygen production by photosynthesis.

Experimentally, a small leaf of *E. densa* was cut with a clean blade and placed between glass coverslips. The space around the leaf, between the coverslips was filled with water to maintain normal processes in the leaf. Chlorophyll has a strong absorption band in the blue and red light regions, so a white light lamp was used to excite the sample. A video record of the sample shows oxygen being released from the leaf, as illustrated in Figure 22. Observation of oxygen means that the plant is producing glucose at the same time.

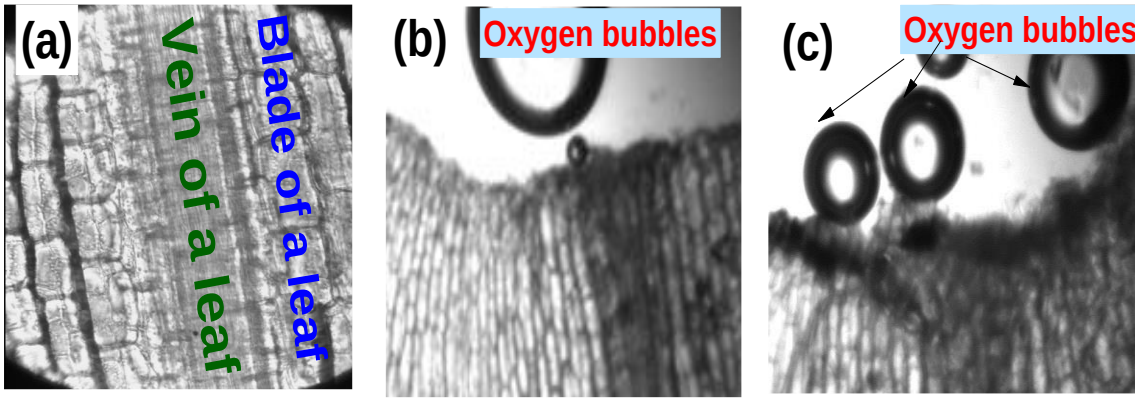

Figure 22: A leaf of *E. densa* plant under the microscope. (a) Optical Image of small spot of *E. densa*'s leaf. (b and c) show that oxygen was produced when the light was on.

4.6 CONCLUSION

In conclusion, the UCNPs were taken up by the root all the way to the stem and leaves as seen in figure (20 b, c, and d). Next step is to use the UCNPs to sense glucose in the plant. Also, by choosing *E.densa* as a model for sensing glucose and/or oxygen, our preliminarily results showed that we can easily detect the photosynthesis by detection of the oxygen that produces during the photosynthesis. Later, we will use *E. densa* for sensing glucose after feeding it with UCNPs.

CHAPTER V

ERYTHROCYTE MEMBRANES LOADED WITH HIGH CONTRAST FLUORESCENT MARKERS

5.1 INTRODUCTION

Erythrocytes, red blood cells, (RBCs) have several unique properties (mobility, abundance and carrying capacity) which make them attractive as a platform for glucose sensing and for drug delivery in animals and humans. Erythrocytes membranes have been used in drug delivery because they can mimic healthy red blood cells [64, 65]. RBCs normally are filled with hemoglobin (Hb) [66], which can be removed and the emptied cell membranes filled [67] with UCNPs. Conventional fluorescent markers such organic dyes and quantum dots have been used to map RBCs membranes' movements for *in vivo* bio-imaging [65, 68], however, they are limited by photostability and toxicity. To overcome these drawbacks, upconversion nanoparticles (UCNPs) and NIR color centers in fluorescent nanodiamonds such as silicon vacancy (SiV) and Nickel vacancy (NiV) can be used. They are ideal for *in vivo* imaging because work in a spectral region of minimal light absorption by Hb (<650 nm) and water (>900 nm). In this work, we first stained RBCs with R6G dye. Later, UCNPs and NIR diamond color centers into empty erythrocytes membranes. This second experiment of loading with biocompatible fluorescent markers is an essential step toward fascinating bioapplications. One can think of using our lanthanide-doped UCNPs with vanadium oxide (VO_4) as cores or core/shells sensitive and selective glucose monitors and for drug-delivery for type 1 and type 2 diabetes by loading ensembles of UCNPs into intact RBC membranes or by coating each UCNP with a red blood cell membrane. Then,

the particles can be excited with a NIR laser to measure glucose in real time in the blood without any background biofluorscence.

5.2 RHODAMINE 6G (R6G)-STAINED RED BLOOD CELLS

Optical imaging of biological cells is an important, but challenging, problem due to weak signals, large background, spectral congestion, reduced contrast, laser-induced photodamage and heating effects. Staining with fluorescent dyes often helps to improve the imaging contrast and to achieve a high spatial resolution in fluorescence microscopy. Also, intrinsic vibrational signals of cells or staining with Raman marker molecules may be used for bioimaging based on Raman microscopy [69]. Both of these complementary techniques benefit from high-intensity lasers which pose a problem of possible laser-induced sample damage and disruption of biological functions. The main challenge is the desirable, dual task of simultaneous imaging and damage-monitoring in a single experiment using one laser. We reach that goal by selecting a rhodamine 6G-stained red blood cell (R6G-stained RBC) for simultaneous fluorescence and resonance Raman imaging using a 532 nm laser excitation. We developed a corresponding data-processing algorithm which allows for separating the two spectroscopic signals. We controled the relative intensity of the R6G and RBC signals by varying the excitation laser power and simultaneously monitor the photostability and oxygenation capability of RBC. We observed no significant photodamage or deoxygenation of RBC under the complete photobleaching of R6G. Our approach may be applied to other types of stained cells with appropriate selection of fluorescent dyes and excitation sources. Fluorescence signals are typically orders of magnitude stronger than Raman signals. However, biological systems often lack chemically-specific fluorescence signals in the visible spectral range and require fluorescent dye- staining for improved imaging contrast.

Staining complicates the experimental preparation process and may influence biological functions [70]. On the other hand, Raman spectroscopy is typically label-free, allowing the study of the sample in its native state. Weak Raman signals may be enhanced using methods such as surface enhancement, coherence or electronic resonance effects. Both fluorescence and Raman imaging, benefit from high-intensity lasers, which can lead to laser-induced sample damage and disruption of biological functions. High laser powers are especially useful for super-resolution imaging when the signals originate from nanoscopic sample volumes with few or single molecules of interest [71-75]. To perform bioimaging using these techniques, the effects of laser intensity on the photostability and function of biomolecules and live cells must be precisely determined. The challenges of rapid, nondestructive, optical imaging in biological media require developing new approaches for simultaneous bioimaging of the cell functions and estimation of the cell stability due to possible photodamage and heat.

Here, we perform optical imaging of rhodamine 6G-stained red blood cells (R6G-stained RBCs), a relatively simple bioimaging system, using a combination of fluorescence and resonance Raman scattering. R6G is a typical fluorescent dye used for staining of biological systems [76, 77]. It is also a typical Raman reporter molecule used for improving the Raman imaging contrast and as a Raman marker in biosensing [78-81]. R6G was specifically chosen because its fluorescence and resonant Raman signals are both relatively strong and may be obtained using 532 nm laser excitation. These strong signals enabled R6G's use as a laser dye and the first Raman spectrum of a single molecule via surface enhancement [82]. Fluorescence of R6G was used in super-resolution optical imaging [83].

We selected a simple biological cell, RBC, whose main constituent protein component, hemoglobin (Hb), provides a strong resonance Raman signal upon 532 nm laser excitation which coincides with the fluorescence and resonance Raman signals of R6G. By staining the RBC with R6G, we designed a stained biological model system which can be used for multi-component bioimaging within a single experimental setup using a single excitation source. This approach allows simultaneous exploration of several effects including fluorescence and resonance Raman bleaching of the stain, and photostability and functional imaging of the biological system. RBCs are critical to the transport of oxygen to the cells in the body. They provide an ideal platform to study oxygenation capability using resonance Raman spectroscopy [84-87]. Laser-induced photodamage and heat effects in RBC have also been probed using Raman spectroscopy [88]. Various excitation sources with wavelengths from the near-UV to near IR were previously used [64, 89, 90]. Our 532 nm excitation matches the electronic resonance transitions in both R6G and Hb, and, therefore, provides the optimal resonance enhancement of the Raman signals of both R6G and RBC. This is accompanied by the simultaneous bleaching of the fluorescence of R6G, which can be gradually controlled and monitored by tuning the laser intensity. Using this control parameter, we detected Hb Raman signals in the presence of the active R6G fluorescence, and R6G Raman signals in the presence of a strong Hb Raman contribution. Since R6G forms a monolayer on the surface of RBCs, its Raman signal is weak compared to Hb. Also, since R6G has a larger absorption coefficient and faster bleaching kinetics [91] than Hb, the bleaching of both fluorescence and resonance Raman signals of R6G are achieved before any noticeable changes in the Raman spectra of Hb occur. The competition between these resonant signals allows the detection of R6G and Hb in the RBCs under various conditions

while probing the photostability of stained RBCs. These results provide a step towards improving real-time multicomponent cellular imaging with high stability and resolution.

5.2.1 MATERIALS AND METHODS

Bovine blood was provided by the Veterinary Medical Park, TAMU. After mixing the blood bag, 5 ml of the bovine blood was placed into a 15 ml tube. The blood was centrifuged at 9000 rpm for 5 min. The supernatant and a buffy coat were discarded and RBCs re-suspended in 10 ml of phosphate-buffered saline (PBS). Again, RBCs were centrifuged (9000 rpm for 3 min) and the supernatant discarded. The preparation of R6G-stained RBCs was performed by mixing the solutions of RBCs with the 1 mM R6G. During this process, R6G adsorbs onto the RBC membrane to form stained cells having both Hb and R6G components. Finally, the R6G-stained RBCs were air dried on a glass substrate and used for imaging either immediately (referred to as fresh cells) or after the 1-week storage (referred to as 1-wk-old cells). The 1-wk -old cells were used for the investigation of the effects of the laser power dependence on the photodamage and oxygenation during imaging. One-week-long storage eliminated the possibility of short-term (several hours) oxygenation changes due to the cell equilibration under the ambient conditions after the preparation.

We performed spectroscopic measurements using a confocal Raman microscope (LabRAM HR Evolution, Horiba) with a 532 nm excitation laser. Schematic of the R6G-stained RBC preparation is shown in Figure 23 (a). The optical microscope images of a typical RBC and R6G-stained RBC are shown in Figure 23 (b and d), respectively. The measured spectra of the RBC and R6G-stained RBC are shown in Figure23 (c and e), respectively. These spectra were obtained by integrating over the whole area of the cell. The typical RBC donut shape is seen in the optical image. The R6G-stained RBCs had a shallower donut shape possibly due to the stress induced during the staining process.

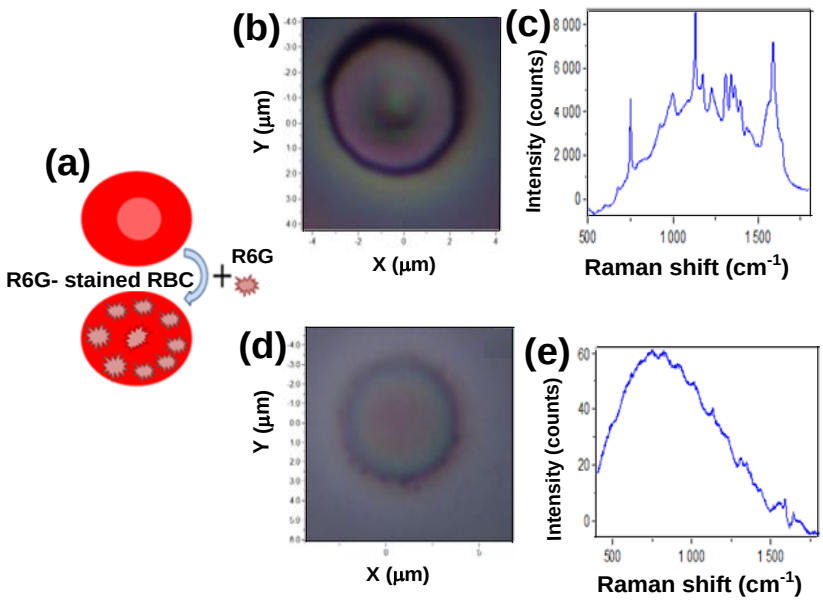

Figure 23: (a) Schematic of the R6G-stained RBC preparation. Optical microscope images (b, d) and spectra (c, e) of RBC and R6G-stained RBCs. The spectrum of RBC is dominated by the resonant Raman signal of Hb, whereas the spectrum of R6G-stained RBC is dominated by the fluorescence of R6G (at low laser power).

5.2.2 RESULTS AND DISCUSSION

We selected the 1-week-old cells to avoid the effects of early aging and to achieve equilibrium for the R6G cell surface adsorption process. Due to the relative weakness of the Raman signals, the complete acquisition of optical images may take up to several hours for one map which has to be repeated several times for different laser powers. The total process of data collection for one cell may take up to several days. Therefore it is desirable to select a cell which is already aged for a week. It was previously reported that the lifetime of typical RBC is several months.

We also performed measurements of RBC older than one week and observed evident aging effects in 2-week-old RBC (data not shown and not used in this work).

To evaluate the photostability of the stained cells, we performed optical measurements on 1-week-old R6G-stained RBC using 532 nm laser excitation. Figure 24 shows the corresponding fluorescence and Raman spectra obtained with 1 sec accumulation time at 0.2 μW (m), 2 μW (n), 20 μW (o), 75 μW (p), 200 μW (q), and 300 μW (r) laser powers. The spectra were integrated over the whole cell and showed a large contribution of the R6G fluorescence at low laser powers and a gradual transition into the bleached spectra with the large contribution of Hb and R6G Raman signals at high powers. The corresponding extracted fluorescence and Raman (1590 cm^{-1} band) images of the 1-week- old stained cell at 1 sec accumulation time in the range of the available laser powers are shown in Figure 24. The band assignment for the resonance Raman spectra of RBCs [89, 92, 93] and R6G [94] of the control unstained fresh RBC and 1-week-old R6G-stained RBC for different laser powers are shown in table 2.

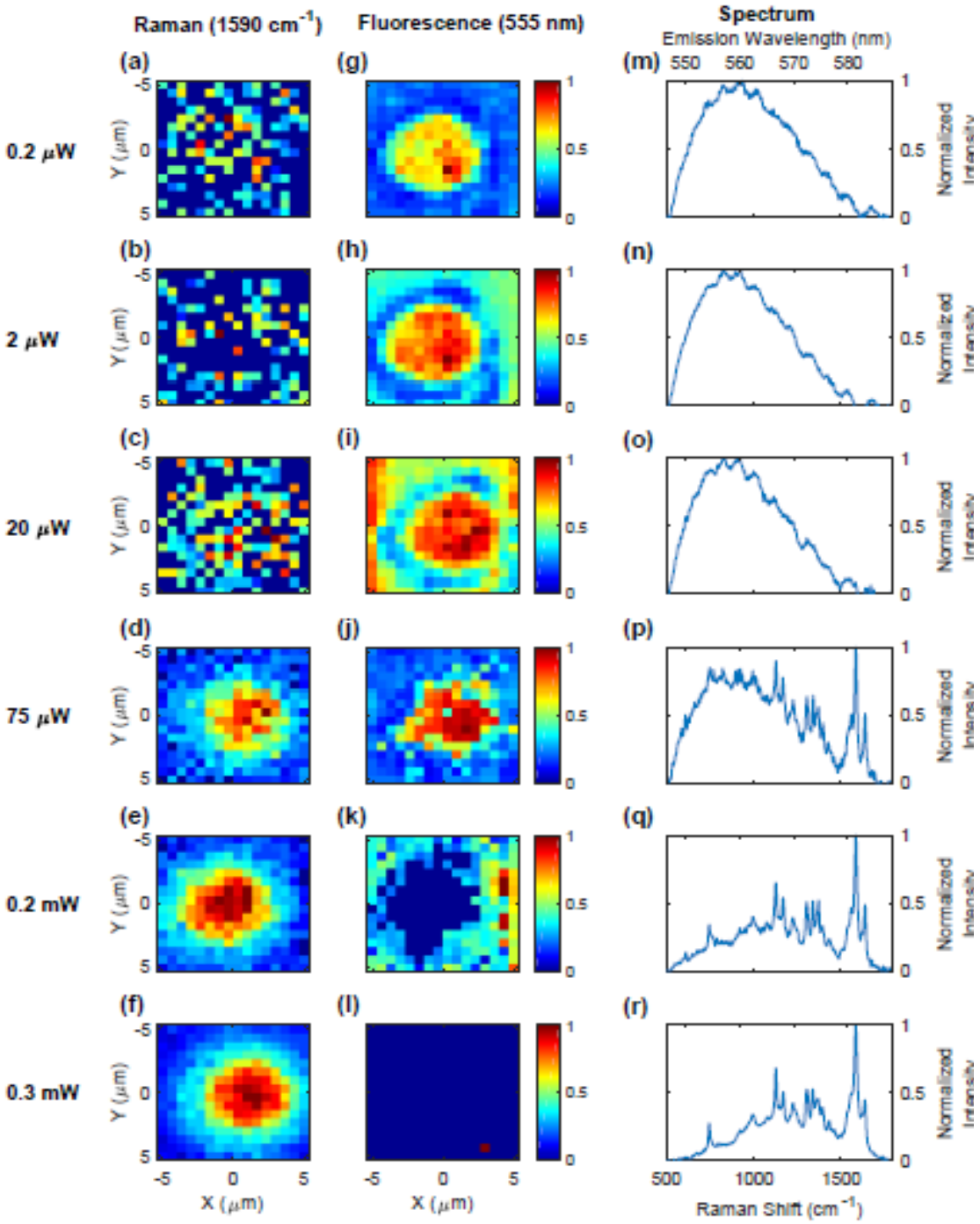

Figure 24: Raman spectra ((m) – (r)) and maps of the 1-week old R6G-stained RBC obtained by integrating the Raman spectral intensity of the 1589 cm-1 band ((a) – (f)) and of the R6G fluorescence ((g) – (l)) at 1 sec accumulation time with different laser powers.

Table 2: Band assignment for the resonance Raman spectra of the control unstained fresh RBC, and 1-week-old R6G-stained RBC for different laser powers. (Abbreviation: ν in plane mode, ϒ out of plane mode, str: stretching.

Peak no.	Raman Band Position of Unstained fresh RBC (cm^{-1})at laser power 75 µW	Raman Band Position of R6G- stained fresh RBC (cm^{-1}) at laser power 75 µW	Raman Band Position of Fresh R6G-stained RBC (cm^{-1}) at laser power 300µW	Raman Band Position of 1 week old R6G-stained RB (cm^{-1}) at laser power 75µW	Raman Band Position of 1 week old R6G stained RBC(cm^{-1}) at laser power 300 µW	Raman Band Position of 1 week old R6G-stained RBC (cm^{-1})at laser power 900 µW	Band assignment for RBC (cm^{-1})	Band assignment for R6G (cm^{-1})
1	750	744	750	747	747	746	ν_{15} , Υ_1	
2	755	755	755	760	760	760	ν_{15} , Υ_1	
3	766	771	766	771	773	771		C-H op bend
4	1133	1133	1135	1129	1128	1128	ν_5	C-H ip bend
5	1150	1140	1141	1145	1146	1145		
6	1161	1153	1159	1154	1157	1153	ν_{44}	
7	1177	1175	1176	1170	1171	1170	ν_{30}	
8	1312	1316	1315	1308	1307	1307	ν_{21}	Arom C-C str
9	1344	1350	1348	1343	1340	1340	ν_{41}	
10	1363	1370	1368	1360	1360	1367	ν_4^d	
11	1374	1380	1379	1373	1373	1374	ν_4	
12	1399	1404	1403	1397	1395	1396	ν_{20}	
13	1548	1550	1550	1546	1544	1543	ν_{11}	
14	1563	1568	1568	1563	1561	1562	ν_2	
15	1590	1593	1593	1587	1586	1586	ν_{37}	
16	1625	1625	1625	1625	1625	1625	ν_{10}, ν (C= =C)	
17	1645	1645	1646	1640	1640	1640	ν_{10}	Arom C_C str

5.3 LOADING / COATING RED BLOOD CELL MEMBRANES WITH BRIGHT FLUORESCENCE MARKERS

As an alternative method of using dyes for staining red blood cells, we have investigated upconversion nanoparticles loading into red blood cell membranes.

5.3.1 LOADING INTACT RED BLOOD CELLS MEMBRANES WITH BRIGHT FLUORESCENT PARTICLES

Bovine blood purchased from the Veterinary Medical Park, TAMU, was kept at 4 C. 50 ml of the blood was mixed several times with 1.5 mg of ethylenediaminetetraacetic-acid (EDTA) per ml of blood for anticoagulation. The loading technique used here was a hypotonic method to load intact red blood cell membranes with fluorescent particles as illustrated in Figure 27.

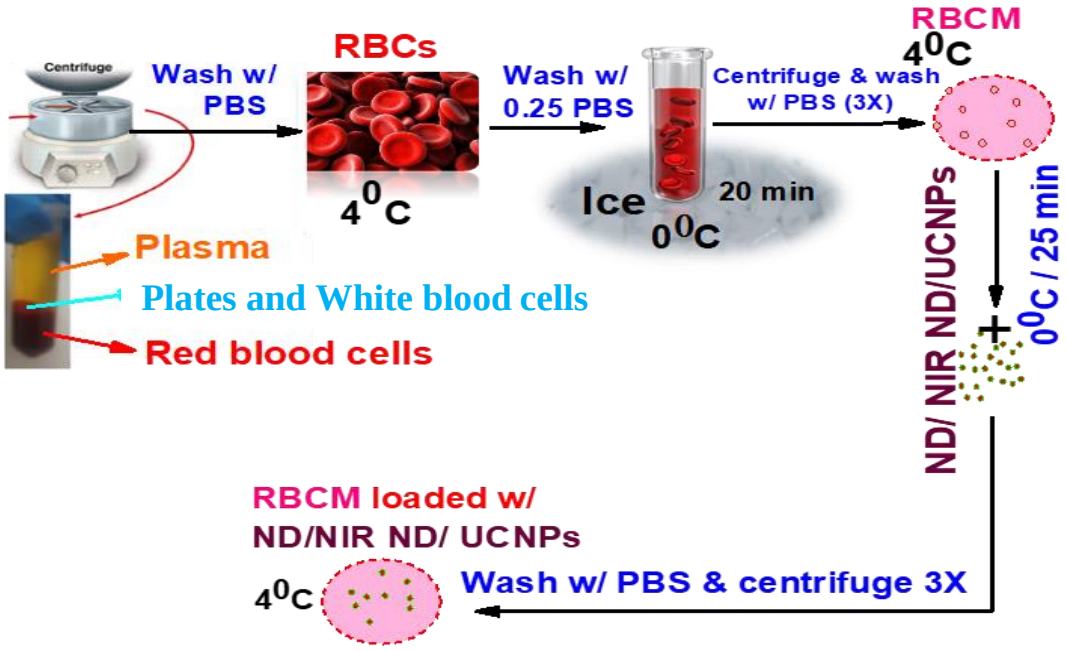

Figure 25: Loading technique of red blood cell membranes with high fluorescent markers.

To do this, we followed a similar procedure as described in [95]. Briefly, 12 ml of whole blood was centrifuged at 9000 rpm for 5 min at 4^0 C to separate red blood cells from the plasma and white blood cells. A buffy coat and the supernatant were discarded, and remaining red blood cells were washed with cold 1 × phosphate buffered saline (PBS) with pH= 7.4 for three times. After this the red blood cells appeared as seen in Figure 26 (a).

Next, for a hypotonic medium treatment, 25% of PBS was added for hemolysis of the RBCs and kept in an ice bath for 20 min. The released hemoglobin was discarded by centrifugation at 9000 rpm for 5 min, and light pinky color of empty RBCs (pellets) as shown in Figure 26 (b) were collected and washed with 100% of PBS three times. Next, 10 mg of UCNPs (YVO_4: Er^{+3}, Yb^{+3} @Nd^{+3}) or nanodiamonds with color centers and 20 µl of R6G solution (nanodiamond data is not presented here) were mixed with 200 µl of the blood in 1 ml of PBS and kept in an ice bath for 25-30 min. After that, by centrifugation and washing with 100% of PBS for three times, the red blood cell membranes (RBCMs) loaded with UCNPs were isolated.

Fluorescent images of these UCNPs-loaded RBC's were obtained using a commercial Zeiss LSM 780 NLO Multiphoton Microscope and Image J software to process. The samples used in this study were not fixed or treated with any other chemicals. To obtain the fluorescent images, a small droplet of the final, loaded cell membranes was placed between microscope glass coverslips (not coated with any chemical and not fixed) to get a very thin layer of the loaded cells. To get fluorescence from the cells loaded with R6G and UCNPs, very low laser power was used at 488 nm, and emission was collected from 550 - 630 nm. The resulting images are seen in Figure 26 (c). Another fluorescence image of the

same sample was taken using a very high power of laser at 808 nm, and the emission was collected from 500- 600 nm as shown in Figure 26 (d). The combination of these two fluorescent images is shown in Figure 26 (e).

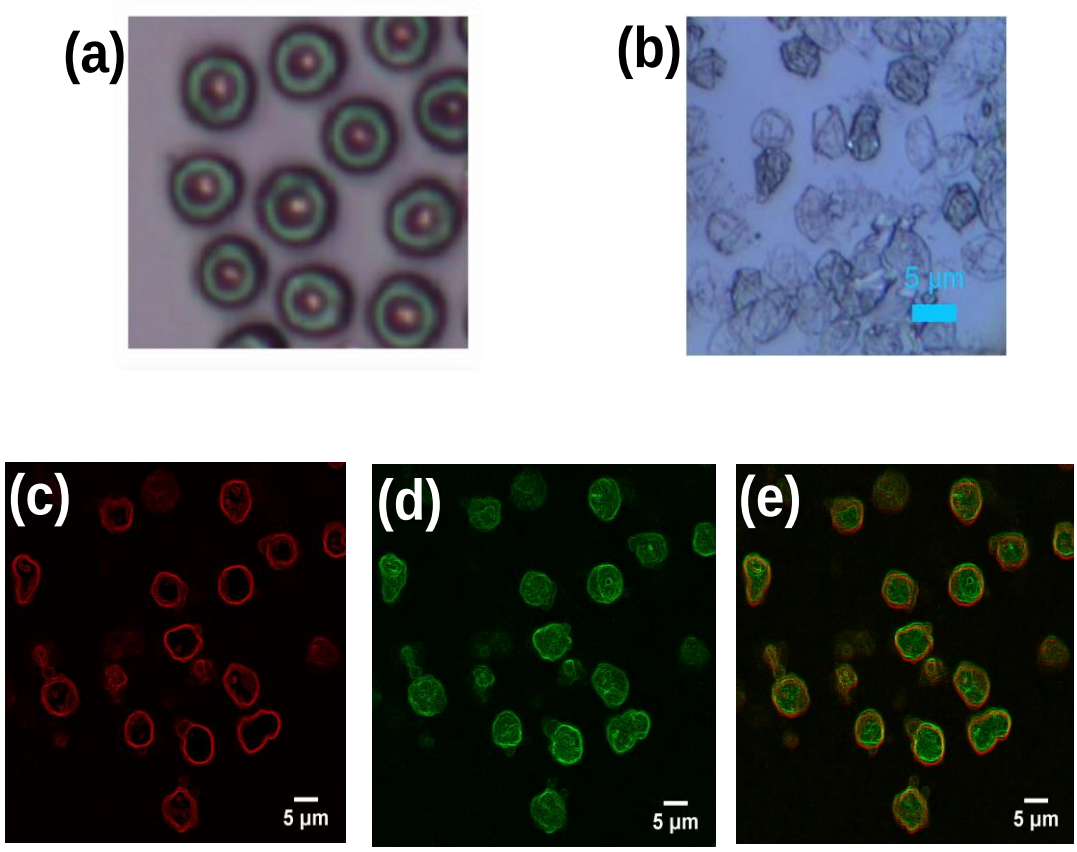

Figure 26: (a) Optical image of control red blood cells under 50X objective. (b) Optical image of red blood cell membranes (RBC ghost). (c) fluorescent image of red blood cells loaded with R6G and UCNPs excited with laser 488 nm and emission collected from 550 -630 nm. (d) Fluorescence image of red blood cells loaded with R6G and UCNPs excited with laser 808 nm emission collected from 500- 600 nm, and (e) combine the fluorescent images for R6G and UCNPs.

Our results indicate that R6G was only found on the edge of the red blood cells which suggests that it was only in the membrane, while UCNPs were found throughout the cells. A very high laser power at 808 nm was used to bleach any R6G so that the only fluorescence in the image was from the UCNPs, not from R6G.

5.3.2 COATING FLUORESCENT NANOPARTICLES WITH RED BLOOD CELL MEMBRANES

Empty RBCs (pellets) were prepared by following the same steps listed above. To coat (encapsulate) UCNPs with red blood cell membranes, a custom-made mini extruder was used. TEM image of UCNPs and the custom-made extruder can be seen in Figure 27 (a and b), respectively. TEM images were obtained with JEM-2010 Electron Microscope. The mixture of 10 μl of red blood cell membranes was mixed with 50 μl of UCNPs in 1 ml of PBS. Then, the mixture was extruded continuously through 200 nm nuclepore polyester membrane using the mini- extruder.

Based on prior work [95] we expect the extruded RBC membranes to reform on the UCNP. To confirm this, TEM and DLS measurements were then made. For this, the final mixture was centrifuged at 10000 rpm for 10 min, and the resulting RBCMs- UCNPs were stored in PBS at 4^0C. The final TEM and dynamic light scattering (DLS) results are shown in Figure 27 (c and d), respectively.

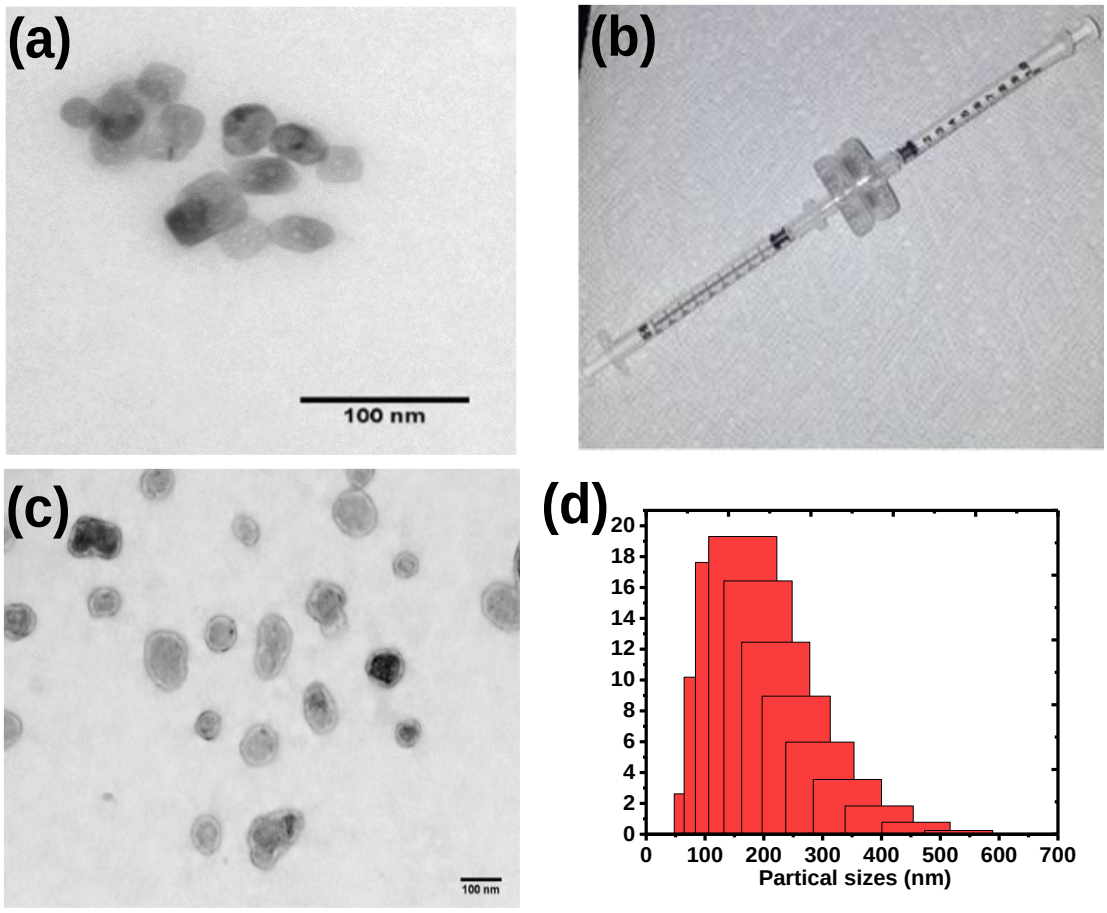

Figure 27: UCNPs coated with red blood cell membranes: (a) TEM image of UCNPs (YVO_4: Er^{+3}, Yb^{+3} @ Nd^{+3}), (b) custom made mini extruder, (c) TEM image of red blood cells membranes encapsulating UCNPs, and (d) Dynamic light scattering (DLS) of UCNPs coated with red blood cell membranes.

5.4 CONCLUSION

From staining red blood cells with R6G, we noticed that the fluorescence intensities decreased by increasing the laser power because R6G photo-bleached gradually. Conversely the Raman lines of hemoglobin dominate at high laser power. The only case where we were able to record both the Raman line from the hemoglobin and fluorescence coming from the dye (R6G) was at 75 μW laser power.

To be able to use red blood cell membranes for drug delivery with the dye as a fluorescence marker the photobleaching must be eliminated. Raman of hemoglobin is not useful because all the red blood cells, even those not loaded with drug, have it. Here, we proposed to use UCNPs as a fluorescent marker to track red blood cell membranes which are used for drug delivery. In this study, we showed that UCNPs can be loaded into red blood cell membranes by using two techniques. First whole membranes were loaded and were almost the same size as native red blood cells. Second, we showed individual UCNPs can be encapsulated with red blood cell membranes and can have any size limited by the particle size. Using UCNPs as fluorescent markers for drug- delivery looks promising since these nanoparticles have no autofluorescence and therefore are good candidates for *in vivo* tracking.

CHAPTER VI

A CUSTOM BUILT CONFOCAL-ATOMIC FORCE MICROSCOPE

6.1 INTRODUCTION

The Atomic Force Microscope (AFM) [96] is a powerful tool for nanoscale imaging with high resolution [97]. Since its invention in 1986 by Gerd Binnig et al. [98], AFM is considered one of the most effective tools that can give an image with very high resolution. AFM can provide a topographic image of a surface. Moreover, it can determine the roughness of a surface sample or measure the thickness of a crystal growth layer. AFM has many applications such as imaging soft biological materials, proteins, and DNA and investigation of properties of single molecules and materials such as graphene.

The fundamental principle of operation for AFM microscopy is to measure the deflection of a microcantilever that has a tip attached to its free end [99]. There is a force acting between the sample and the tip which produces the deflections which can be analyzed during the scan. Typically, these forces work at distances less than or equal to 100 Å such as Van der Waals [100, 101], Coulomb forces and magnetic forces.

First, the interaction force between the tip and the sample starts when the tip approaches the sample due to an extensive range of long-range attractive forces. When the tip is close to the sample, the interaction will increase. However for a very close distance between the atoms of the tip and the sample, the orbital electrons begin to repel (the forces become positive). The forces are canceled if the distance between the sample and the tip is

on the order of some angstroms (i.e., characteristic of a chemical bond). When the sample and the tip are in contact, the repulsive forces dominate.

6.2 AFM OPERATION MODES

There are three modes to operate the AFM: noncontact mode, intermittent or tapping mode and contact mode. Eeach mode operates on different distance regions, as can be seen in Figure 28 (adopted from [102]).

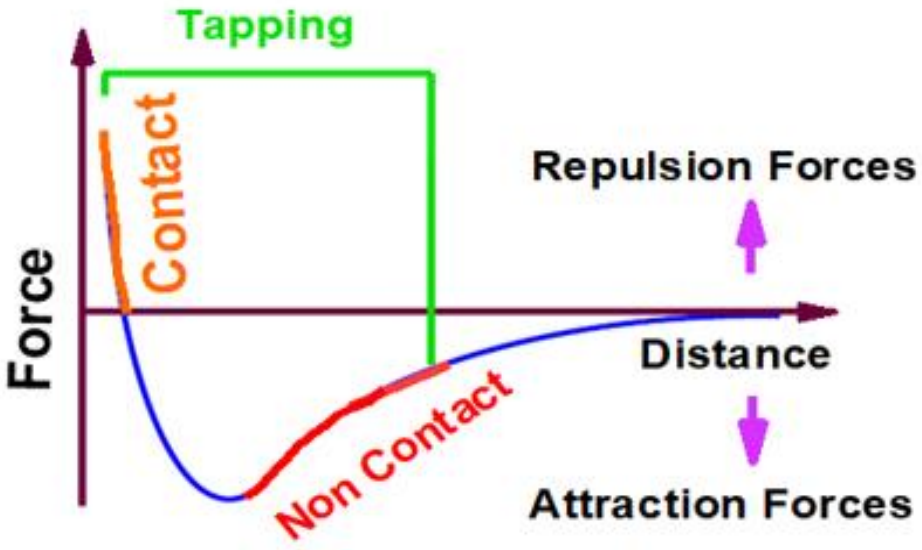

Figure 28: AFM operation modes.

Non-contact mode is used for soft samples, and a vacuum is needed. The distance range is between 50 Å – 150 Å. In tapping mode, the tip is touching the surface gently and

frequently. It is often used for biological samples. It can be used in air or liquid and provides good resolution. In contact mode, the tip is in continuous contact with a sample.

It is preferably used for hard samples and it can be used in air or liquid, and gives a high resolution.

Van Der Waals forces can explain the interaction of the tip and the sample and can be approximated by Lennard-Jones potential, as given by:

$$U(r) = U_0 \left(\left(\frac{r_0}{r} \right)^{12} - 2 \left(\frac{r_0}{r} \right)^{6} \right)$$

The first term describes the short-range repulsion due to Pauli Exclusion Principle and the second term describes the long-distance attraction triggered, mainly, by dipole-dipole interaction. r_0 and U_0represent the parameters of the equilibrium distance between atoms, and the energy value in the minimum, respectively, as in Figure 29.

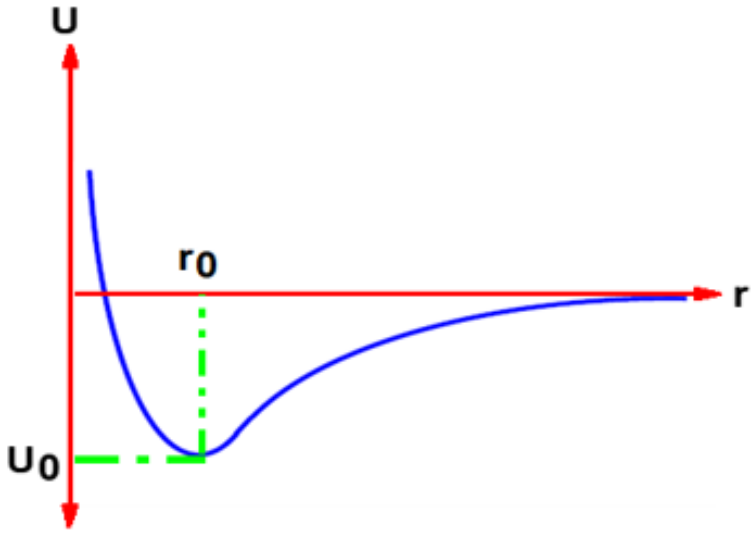

Figure 29: Lennard-Jones potential form.

The interaction force F(r) of a tip with a sample can be estimated using the Lennard-Jones potential:

$$F(r) = -\frac{\partial U}{\partial r}$$

Over the years the AFM has motivated a variety of other scanning probe techniques [103-105]. For example by modifying the tip, it is possible to measure other quantities such as electric and magnetic properties, friction, chemical potentials, and perform various types of spectroscopy and analysis.

6.3 ADVANTAGES AND DISADVANTAGES OF AFM

There are several advantages of AFM such as the measurements do not need difficult sample preparation. It gives accurate height information, and living systems can be studied. AFM can give us 3-D imaging which provides many pieces of information about the studied samples. Moreover, AFM can quantify surface roughness.

However, there are some limitations. For example the AFM image is not independent of the tip, the measurements are limited in the vertical range, and there is a limited magnification range. Also the AFM tip or the sample can be damaged easily and the scanning speed is limited.

6.4 COMMERCIAL VERSUS CUSTOM BUILT AFM

The Nitrogen-Vacancy (NV color center in diamond) is famous for its applications in magnetometry [106, 107]. One way to use NV is as magnetometer probes attached to an AFM. However most commercial AFM-Confocal microscopes cannot see the fluorescence of a single NV or silicon vacancy (SiV) without tip enhanced photoluminesces (TEPL). Moreover, most commercial AFM-Confocal microscopes use a magnetic mount which can interfere with any magnetic measurement. Besides that, when the microscope breaks down, only the company can fix it. All these reasons encouraged us make a custom AFM that can be optimized for purposes such as the study of NV, SiV, (germanium vacancy) GeV and upconversion nanoparticles (UCNPs). By making a custom built AFM we will be able to self-repair and change the configurations of the microscope as needed.

The tip plays a prominent role in the function of the AFM such as magnetic force microscope (MFM) [108]. Custom tips such as glass, platinum Iridium tip (Pt-Ir) or

commercial tips can be used to study different properties of a sample. Moreover, a custom system enables us to add more lasers with different wavelengths to enhance the fluorescence of nanodiamond color centers and upconversion nanoparticles.

6.5 EXPERIMENTAL SETUP

Quartz tuning forks which are commercially available were used to fabricate our AFM tips for several reasons like their high reliability and low cost [109, 110]. The resonance frequency of these quartz tuning forks was 32.768 kHz. In this work, our custom built AFM is working with tapping mode.

To generate an image of the sample's surface, the AFM tip is raster scanned. The tuning fork is connected to a pre-amplifier circuit, And the distance between the tip and the sample surface is maintained with a feedback circuit. The feedback circuit as illustrated in Figure 30.

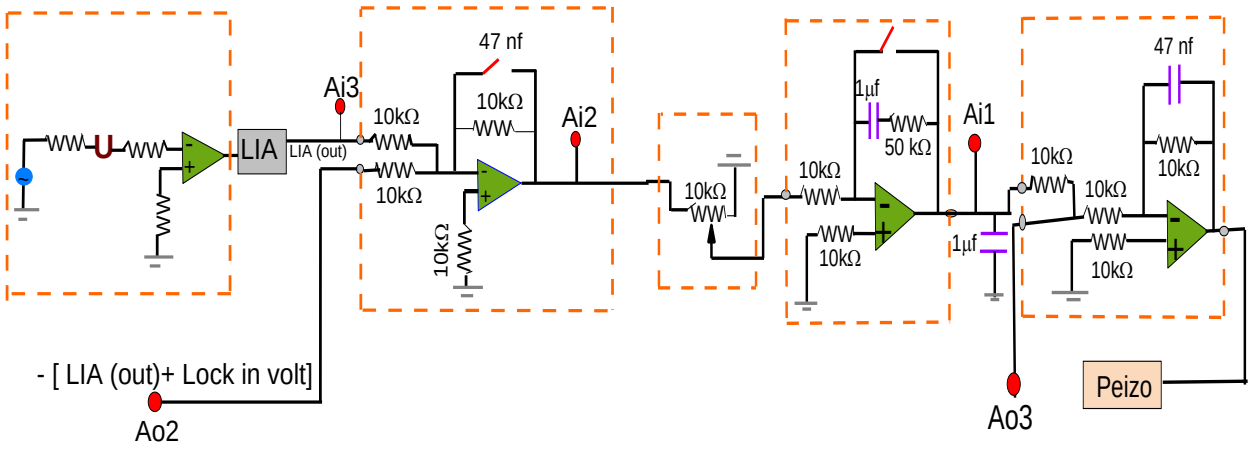

Figure 30: AFM feedback circuit

A tip is glued to the end of one prong of the tuning fork and oscillating perpendicular to the surface of the sample as in Figure 31 (top left). The sample is placed on an XYZ stage with piezo adjustments. The optical access for the confocal microscope is from the bottom of the sample. The objective has 100x magnification and 0.8 numerical aperture (NA), and a considerable work distance. The eexperimental setup of the Confocal-Custom built AFM is shown in Figure 31.

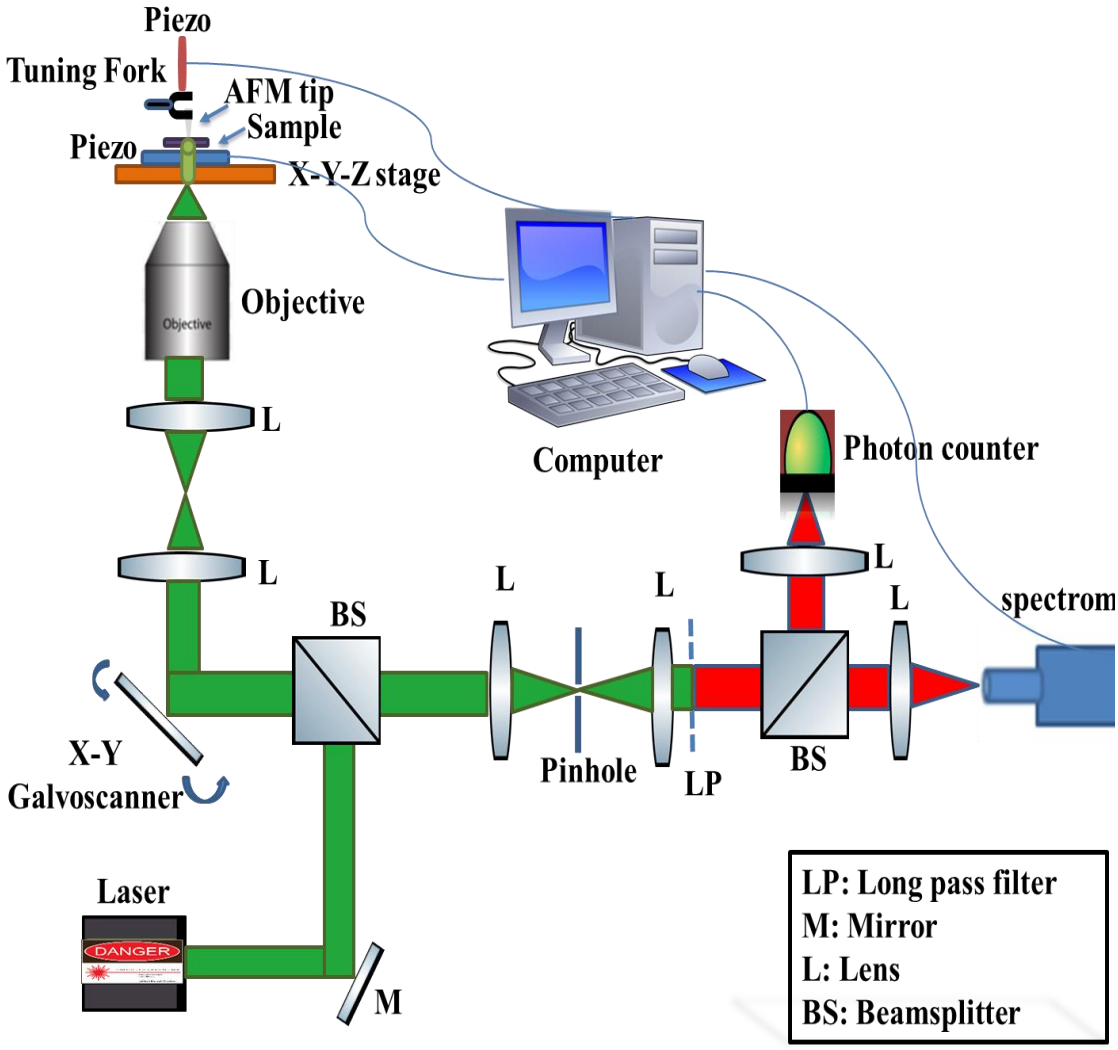

Figure 31: Schematic of Confocal-Custom built confocal- AFM setup.

Figure 32 shows real pictures of the custom-built confocal – AFM setup. The early stages are shown in Figure 32 (a,b and c). Where Figure 32 (a) shows a function generator and an oscilloscope that was used to find the resonance frequency of the tuning fork that later was used to hold the AFM's tip. Figure 32 (b) shows a simple connection for the preamplifier circuit. Figure 32 (c) presents the overview of the AFM in his early stages when it started to make pictures. Part of the confocal setup showing some optics is in Figure 32 (d). Three high voltage amplifier circuits were made to drive the sample via the piezo mount as in Figure 32 (e). The final and current setup of the custom-built AFM is shown in Figure 32 (f).

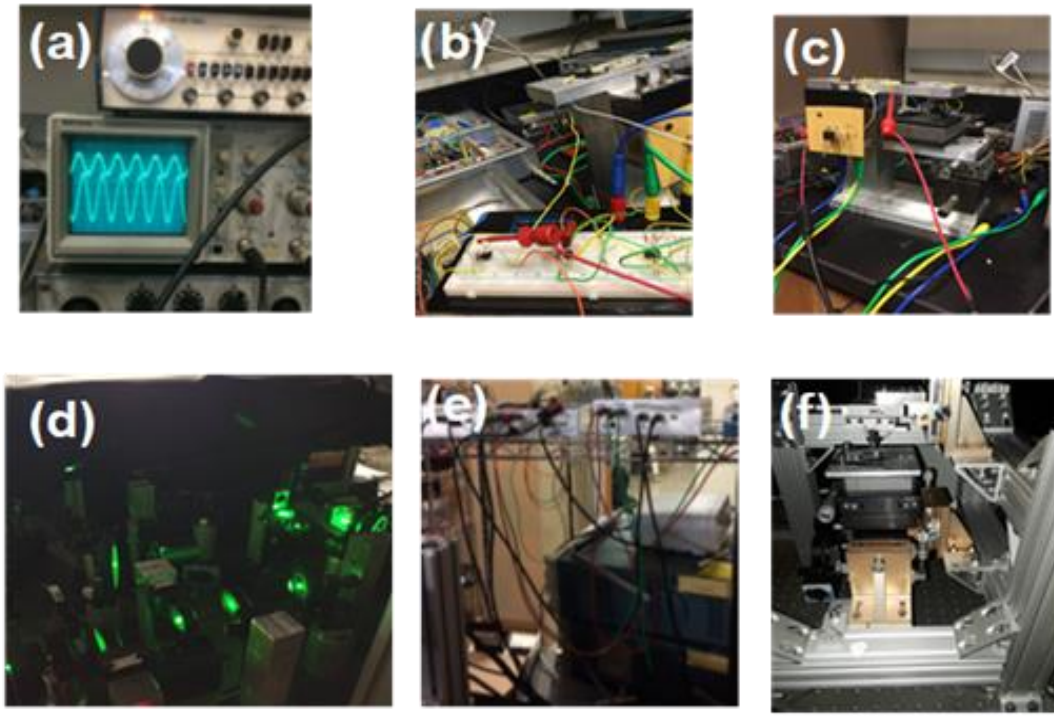

Figure 32: (a,b, and c) show the early stages of the AFM setup, (d) part of the confocal setup, (e) circuits for high voltage amplifier, and (f) current AFM setup.

6.6. FABRICATION OF THE TIPS

6.6.1 AFM GLASS TIPS

A micropipette puller P-87 from SUTTER INSTRUMENT CO. as shown Figure 33 (a), was used to cut the glass tubes and make a sharp glass tip with a size of a few microns as in Figure 33 (b). Resonator and oscillator quartz tuning forks with resonance frequency 32.768 kHz come packed in vacuum, the left image on figure 6c. They were opened to the air as in the right image in Figure 33 (c). The sharp tip of the glass pulled with the micropipette puller was cut carefully using a sharp blade and held using tweezers from the thick edge to keep the sharp edge safe. The glass tip was then glued to one prong of the tuning fork and left to dry for an hour. An AFM glass tip is ready to be used is in Figure 33 (d).

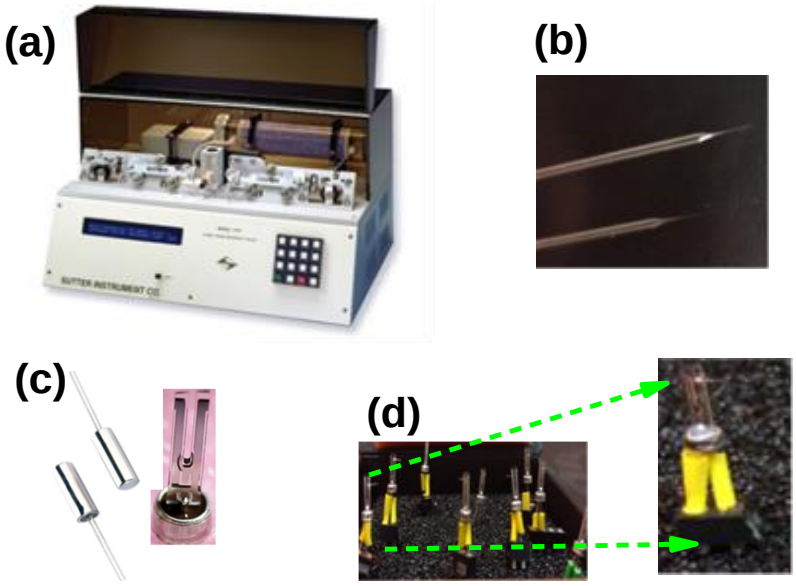

Figure 33: Fabrication of the AFM glass tip: (a) micropipette puller (P-87), (b) glass tube was cut using the micropipette puller, (c) quartz tuning fork in a vacuum(left) and in air (right), and (d) the AFM glass tip.

6.6.2 AFM TIP OF Pt-Ir

Platinum-Iridium wire with diameter 0.127 mm (Alfa-Asear) as shown in Figure 34 (a) was cut by a wire cutter with an angle to make a sharp edge. Then, a sharp part of the wire was cut and held a tweezer with careful handling. The tweezer with the wire was placed on a holder. A quartz tuning fork was opened from its holder (vacuum to air) and was placed on another holder as seen in Figure 34 (b). Next, one edge of the quartz tuning fork was stained with a minimal amount of superglue then the Pt-Ir wire touched the glue and connected to one prong of the tuning fork as in Figure 34 (c). The wire and the tuning fork were left to dry for 1 hour. Then, the AFM Pt-Ir tip was ready.

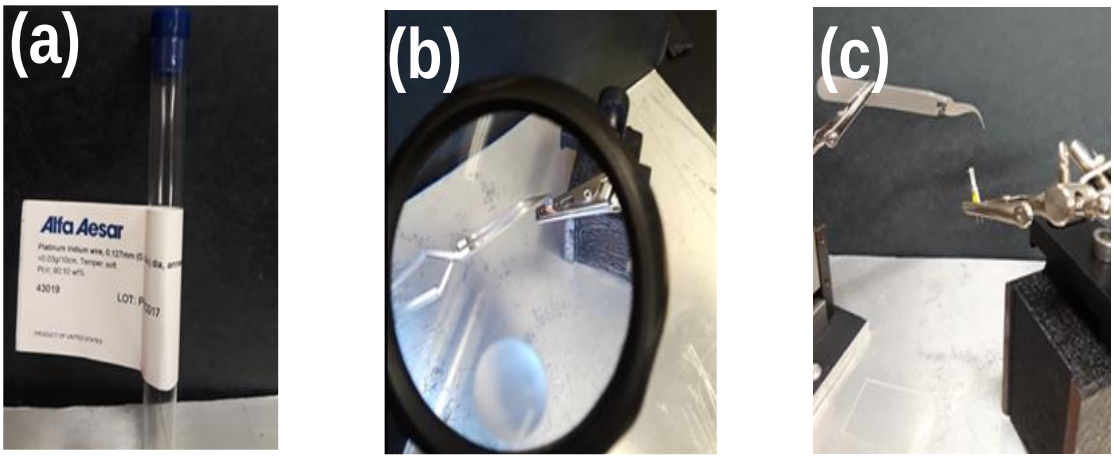

Figure 34: Fabrication of Pt-Ir tip: (a) Pt- Ir wire from Alfa-Aesar, (b) attaching the Pt-Ir wire to one edge of the quartz tuning fork. (c) AFM Pt-Ir is ready to use.

6.7 CUSTOM BUILT CONFOCAL- AFM SETUP RESULTS

A sample of nanodiamond with NV color centers (Admas ~150nm) was spin-coated with PVA (1:1) on a microscope glass coverslip and scanned with AFM glass tip as shown in Figure 35 (a). Figure 35 (a) shows a raw data from the software of the AFM that was written in Python programming language. The fluorescence spectrum of NV of this sample was obtained using the confocal setup. Figure 35 (b) shows fluorescence spectrum (from raw data) of NV. A TEM grid with 2000 mesh was scanned using AFM Pt- Ir tip as shown in Figure 35 (c). Figure 35 (d) shows the sample of TEM grid was stick on a microscopic coverslip and placed on the XYZ stage to be scanned with AFM Pt-Ir tip.

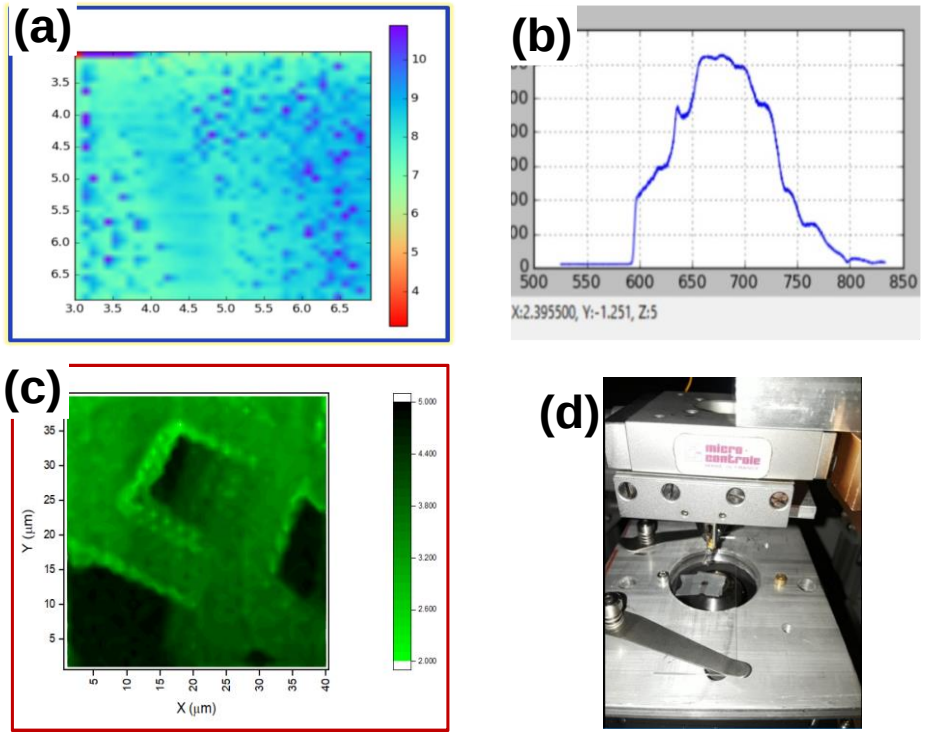

Figure 35: AFM image of Admas ~ 150nm using AFM glass tip. (b) Fluorescence spectrum of NV from the sample Admas ~150 nm. (c) AFM image of TEM grid with 2000 mesh, and (d) Picture for the TEM grid sample.

6.8 CONCLUSION AND FUTURE WORK

The confocal-AFM setup will be used for measuring both the size and the intensities of our nanoparticles at the same time. Having a custom built AFM will give opportunities to use custom made AFM tips such as glass or Pt/Ir. Also, we can modify the AFM to optimize performance for our particles. Because no magnetic a mount was used in the custom built AFM the magnetic sensing capability of nanodiamonds with NV color centers can be studied. Moreover, we can use a commercial AFM tip on the custom built AFM to get high resolution images. The setup is also able to be modified to fit different purposes such as tip enhancement studies.

CHAPTER VII

SUMMARY

Diabetes (Hyperglycemia) is a chronic disease that affects life millions of people worldwide rapidly. Diabetes and hypoglycemia are associated strictly with the glucose level in blood. Blood glucose monitoring is essential to avoid unwanted consequences of glucose level fluctuations. Upconversion nanoparticles (UCNPs) are superior to other optical glucose monitors owing to their photostability, low toxicity, and exceptional autofluorescence suppression. Recently, functionalized upconversion nanoparticles have shown a potential for sensitive monitoring of glucose levels. However, surface functionalization can be easily affected by other factors in the bloodstream, which may also affect their reversibility as shown in chapter I. Therefore, in chapter II, we synthesized and characterized of ($YVO_4: Yb^{+3}, Er^{+3}@Nd^{+3}$, and $GdVO_4: Yb^{+3}, Er^{+3}@Nd^{+3}$) core/shell Upconversion nanoparticles. In chapter III, here, we report YVO_4: Yb^{+3}, Er^{+3}@ Nd^{+3} core/shell UCNPs (average size 20 nm) and $GdVO_4$: Yb^{+3}, $Er^{+3}@Nd^{+3}$ core/shell UCNPs (average size 60- 80 nm without silica-gel treatment during the annealing process), that showed sensitive, reversible and selective optical glucose sensitivity without the need for any surface functionalization or modifications. Comparing with current conventional methods, our upconversion nanoparticles have owned a broad range of sensing glucose which can be used as monitoring for blood glucose levels because it covers all the range needed to monitor glucose levels in the blood as an application as proposed in chapter III. Moreover, the applications of UCNPs can go beyond what was described here. For instance, as described before in chapter IV, our method can be used to sense glucose level in plants,

as well. That gives us an opportunity to develop a new and fast technique to measure glucose levels in plants using upconversion nanoparticles. At the same time, we can use NV sensors of oxygen as an indirect way to measure the glucose level and/or combine both techniques in a hybrid bimodal sensor to avoid any confusion. Another application besides their ability to monitor glucose level, one can think of using our UCNPs of lanthanide ions doped in vanadium oxide (VO_4), which show high sensitivity and selectivity to glucose, as drug delivery to type 1 and type 2 diabetes by loading or coating them with red blood cells (Erythrocytes) membrane. There are several properties of red blood cells make them attractive as a platform for drug delivery and a blood glucose sensing as well such as their mobility, carrying capacity and large quantity. Conventional fluorescent markers such as organic dyes and quantum dots are used to map RBCs membranes movements' *in vivo* bio-imaging. However, organic dyes and quantum dots are limited by photostability and toxicity. To overcome these offsets, upconversion nanoparticles (UCNPs) and near-infrared (NIR) color centers in fluorescent nanodiamonds such as silicon vacancy (SiV) centers and Nickel vacancy (NiV) centers are used due to their background suppression and photostability. These are ideal for in vivo imaging because of minimal light absorption by hemoglobin and water. In this work, we introduced UCNPs and NIR color centers in NDs into Erythrocytes membranes. This loading with biocompatible fluorescent markers is a remarkable step toward important applications in biology as explained in chapter V.

To optimize our custom made nanoparticles which proposed here as a biosensor and some bio-imaging applications, we need to study their characterization such as their brightness and sizes, the need to have a custom built confocal-AFM become as essential as in chapter VI.

REFERENCES

[1] H. Wang, J. Yi, Y. Yu, and S. Zhou, "NIR Upconversion Fluorescence Glucose Sensing and Glucose-Responsive Insulin Release of Carbon Dot- Immobilized Hybrid Microgels at Physiological pH," *Nanoscale,* vol. 9, no. 2, pp. 509-516, 2017.

[2] "National Diabetes Fact Sheet: National Estimates and General Information on Diabetes and Prediabetes, U.S. Department of Health and Human Services, Centers for Disease Control and Prevention," *Atlanta, GA.,* Report 2012, 2012.

[3] M. Zhang, C. Liao, C. H. Mak, P. You, C. L. Mak, and F. Yan, "Highly Sensitive Glucose Sensors Based on Enzyme-Modified Whole-Graphene Solution-Gated Transistors," *Sci Rep,* vol. 5, pp. 8311, 2015.

[4] E. H. Yoo and S. Y. Lee, "Glucose Biosensors: An Overview of Use in Clinical Practice," *Sensors",* vol. 10, no. 5, pp. 4558-76, 2010.

[5] P. Damborsky, J. Svitel, and J. Katrlik, "Optical Biosensors," *Essays Biochem,* vol. 60, no. 1, pp. 91-100, 2016.

[6] S. M. B. a. O. S. Wolfbeis, "Optical Biosensors," *Chem. Rev. ,* vol. 108, pp. 423−461, 2008.

[7] H. Wang, J. Yi, D. Velado, Y. Yu, and S. Zhou, "Immobilization of Carbon Dots in Molecularly Imprinted Microgels for Optical Sensing of Glucose at Physiological pH," *ACS Applied Materials & Interfaces,* vol. 7, no. 29, pp. 15735-15745, 2015.

[8] H. E. Koschwanez and W. M. Reichert, "*In vitro, in vivo* and Post Explantation Testing of Glucose-Detecting Biosensors: Current Methods and Recommendations," *Biomaterials,* vol. 28, no. 25, pp. 3687-703, 2007.

[9] J. Durner, "Clinical Chemistry: Challenges for Analytical Chemistry and the Nanosciences from Medicine,", *Angew Chem Int Ed Engl,* vol. 49, no. 6, pp. 1026-51, 2010.

[10] J. S. Hansen and J. B. Christensen, "Recent Aadvances in Fluorescent Arylboronic Acids for Glucose Sensing," *Biosensors,* vol. 3, no. 4, pp. 400-18, 2013.

[11] Xinjie Zhang,a Chunmei Gao, Shaoyu L¨u, Haogang Duan, Nannan Jing, Di Dong, Caifeng Shia and Mingzhu Liu, "Anti-Photobleaching Flower-Like Microgels as Optical Nanobiosensors with High Selectivity at Physiological Conditions for Continuous Glucose Monitoring," *Journal of Materials Chemistry B,* vol. 2, no. 33, pp. 5452-5460, 2014.

[12] M. Mesch, C. Zhang, P. V. Braun, and H. Giessen, "Functionalized Hydrogel on Plasmonic Nanoantennas for Noninvasive Glucose Sensing," *ACS Photonics,* vol. 2, no. 4, pp. 475-480, 2015.

[13] W. Wu, N. Mitra, E. C. Y. Yan, and S. Zhou, "Multifunctional Hybrid Nanogel for Integration of Optical Glucose Sensing and Self-Regulated Insulin Release at Physiological pH," *ACS Nano,* vol. 4, no. 8, pp. 4831-4839, 2010.

[14] W. Wu, T. Zhou, J. Shen, and S. Zhou, "Optical Detection of Glucose by CdS Quantum Dots Immobilized in Smart Microgels," *Chemical Communications,* vol. 14, no. 29, pp. 4390-4392, 2009.

[15] Y. Li and S. Zhou, "Facile One-Pot Synthesis of Organic Dye-Complexed Microgels for Optical Detection of Glucose at Physiological pH," *Chemical Communications,* vol. 49, no. 49, pp. 5553-5555, 2013.

[16] D. Wang, T. Liu, J. Yin, and S. Liu, "Stimuli-Responsive Fluorescent Poly(N-isopropylacrylamide) Microgels Labeled with Phenylboronic Acid Moieties as Multifunctional Ratiometric Probes for Glucose and Temperatures," *Macromolecules,* vol. 44, no. 7, pp. 2282-2290, 2011.

[17] Hui Wang, Anton Mararenko, Guixin Cao, Zheng Gai, Kunlun Hong, Probal Banerjee, and Shuiqin Zhou , "Multifunctional 1D Magnetic and Fluorescent Nanoparticle Chains for Enhanced MRI, Fluorescent Cell Imaging, and Combined Photothermal/Chemotherapy," *ACS Applied Materials & Interfaces,* vol. 6, no. 17, pp. 15309-15317, 2014.

[18] V. I. Shubayev, T. R. Pisanic, 2nd, and S. Jin, "Magnetic Nanoparticles for Theragnostics," *Adv Drug Deliv Rev,* vol. 61, no. 6, pp. 467-77, 2009.

[19] T. R. Pisanic, 2nd, J. D. Blackwell, V. I. Shubayev, R. R. Finones, and S. Jin, "Nanotoxicity of Iron Oxide Nanoparticle Internalization in Growing Neurons," *Biomaterials,* vol. 28, no. 16, pp. 2572-81, 2007.

[20] Yu Pan, Sabine Neuss, Annika Leifert, Monika Fischler, Fei Wen, Ulrich Simon, G-nter Schmid, Wolfgang Brandau, and Willi Jahnen-Dechent , "Size-Dependent Cytotoxicity of Gold Nanoparticles," *Small,* vol. 3, no. 11, pp. 1941-9, 2007.

[21] K. Schenke-Layland, I. Riemann, O. Damour, U. A. Stock, and K. König, "Two-Photon Microscopes and *in vivo* Multiphoton Tomographs — Powerful Diagnostic Tools for Tissue Engineering and Drug Delivery," *Advanced Drug Delivery Reviews,* vol. 58, no. 7, pp. 878-896, 2006.

[22] J. Chen and J. X. Zhao, "Upconversion Nanomaterials: Synthesis, Mechanism, and Applications in Sensing," vol. 12, no. 3, pp. 2414-35, 2012.

[23] Can T. Xu1, Qiuqiang Zhan, Haichun Liu, Gabriel Somesfalean, Jun Qian, Sailing He, and Stefan Andersson-Engels "Upconverting Nanoparticles for Pre-Clinical diffuse optical imaging, microscopy and sensing: Current trends and future Challenges," *Laser & Photonics Reviews,* vol. 7, no. 5, pp. 663-697, 2013.

[24] Jing Yuan, Yao Cen, Xiang-Juan Kong, Shuang Wu, Chen-Liwei Liu, Ru-Qin Yu, and Xia Chu , "MnO_2-Nanosheet-Modified Upconversion Nanosystem for Sensitive Turn-On Fluorescence Detection of H_2O_2 and Glucose in Blood," *ACS Applied Materials & Interfaces,* vol. 7, no. 19, pp. 10548-10555, 2015.

[25] X. Xie, N. Gao, R. Deng, Q. Sun, Q.-H. Xu, and X. Liu, "Mechanistic Investigation of Photon Upconversion in Nd^{+3}-Sensitized Core–Shell Nanoparticles," *Journal of the American Chemical Society,* vol. 135, no. 34, pp. 12608-12611, 2013.

[26] Y. F. Wang, G. Y. Liu, L. D. Sun, J. W. Xiao, J. C. Zhou, and C. H. Yan, "$Nd(^{3+})$-Sensitized Upconversion Nanophosphors: Efficient *in vivo* Bioimaging Probes with Minimized Hheating Effect," *ACS Nano,* vol. 7, no. 8, pp. 7200-6, 2013.

[27] Hongyu Lu, Haoyue Hao, Guang Shi, Yachen Gao, Ruixue Wang,Yinglin Song, Yuxiao Wang and Xueru Zhang, " Optical Temperature Sensing in β-$NaLuF_4$:Yb^{+3}/ Er^{+3}/Tm^{+3} Based on Thermal, Quasi-Thermal and Non-Thermal Coupling Levels," *RSC Advances,* vol. 6, no. 60, pp. 55307-55311, 2016.

[28] O. A. Savchuk, J. J. Carvajal, C. Cascales, J. Massons, M. Aguilo, and F. Diaz, "Thermochromic Upconversion Nanoparticles for Visual Temperature Sensors with High Thermal, Spatial and Temporal Resolution," *Journal of Materials Chemistry C,* vol. 4, no. 27, pp. 6602-6613, 2016.

[29] Xingjun Zhu, Wei Feng, Jian Chang, Yan-Wen Tan, Jiachang Li, Min Chen, Yun Sun and Fuyou Li, "Temperature-Feedback Upconversion Nanocomposite for Accurate Photothermal Therapy at Facile Temperature," *Nature Communications,* vol. 7, pp. 10437, Feb 4 2016.

[30] T. V. Gavrilović, D. J. Jovanović, V. Lojpur, and M. D. Dramićanin, "Multifunctional Eu^{3+}- and Er^{3+}/Yb^{3+}-Doped $GdVO_4$ Nanoparticles Synthesized by Reverse Micelle Method," *Scientific Reports,* Article vol. 4, p. 4209, 2014.

[31] Masfer Alkahtani, Yunyun Chen,Julie J. Pedraza, Jorge M. González, Dilworth Y. Parkinson, Philip R. Hemmer, and Hong liang, "High Resolution Fluorescence Bio-Imaging Upconversion Nanoparticles in Insects," *Optics Express,* vol. 25, no. 2, pp. 1030-1039, 2017.

[32] M. Alkahtani, L. Jiang, R. Brick, P. Hemmer, and M. Scully, "Nanometer-Scale luminescent Thermometry in Bovine Embryos," *Optics Letters,* vol. 42, no. 23, pp. 4812-4815, 2017.

[33] T. Scior, J. A. Guevara-Garcia, Q. T. Do, P. Bernard, and S. Laufer, "Why Antidiabetic Vanadium Complexes are Not in the Pipeline of "Big Pharma" Drug Research? A Critical Review," *Curr Med Chem,* vol. 23, no. 25, pp. 2874-2891, 2016.

[34] E. Kioseoglou, S. Petanidis, C. Gabriel, and A. Salifoglou, "The Chemistry and Biology of Vanadium Compounds in Cancer Therapeutics," *Coordination Chemistry Reviews,* vol. 301-302, pp. 87-105, 2015.

[35] L. Zhang , Y. Zhang , Q. Xia b, X.M. Zhao , H.X. Cai , D.W. Li , X.D. Yang, K. Wang, Z.L. Xi, "Effective Control of Blood Glucose status and toxicity in streptozotocin-induced diabetic rats by orally administration of vanadate in an herbal decoction," *Food Chem Toxicol,* vol. 46, no. 9, pp. 2996-3002, 2008.

[36] Mialon, G. Mialon, S. Türkcan, A. Alexandrou, T. Gacoin, and J. P. Boilot, "New Insights into Size Effects in Luminescent Oxide Nanocrystals," *The journal of physical chemistry. C,* vol. 113, no. 43, pp. 18699-18706, 2009.

[37] Genevie`ve Mialon, Silvan Tu¨rkcan, Ge´raldine Dantelle, Daniel P. Collins, Maria Hadjipanayi, Robert A. Taylor,Thierry Gacoin, Antigoni Alexandrou, and Jean-Pierre Boilot, "High Up-Conversion Efficiency of YVO_4:Yb,Er Nanoparticles in Water down to the Single-Particle Level," *The Journal of Physical Chemistry C,* vol. 114, no. 51, pp. 22449-22454, 2010.

[38] G. Mialon, S. Türkcan, A. Alexandrou, T. Gacoin, and J. P. Boilot, "New Insights into Size Effects in Luminescent Oxide Nanocrystals," *The Journal of Physical Chemistry C,* vol. 113, no. 43, pp. 18699-18706, 2009.

[39] H. A. Masfer, S. A. Fahad, S. Carlos, L. G. Carmen, L. Hong, and R. H. Philip, "High Efficiency Upconversion Nanophosphors for High-Contrast Bioimaging," *Nanotechnology,* vol. 27, no. 48, pp. 485501, 2016.

[40] P. Shen and Y. Xia, "Synthesis-Modification Integration: One-Step Fabrication of Boronic Acid Functionalized Carbon Dots for Fluorescent Blood Sugar Sensing," *Anal Chem,* vol. 86, no. 11, pp. 5323-9, 2014.

[41] H. Charles J. Godfray, John R. Beddington, Ian R. Crute, Lawrence Haddad, David Lawrence, James F. Muir, Jules Pretty, Sherman Robinson, Sandy M. Thomas, Camilla Toulmin, "Food Security The Challenge of Feeding 9 Billion People," *SCIENCE,* vol. 327, no. 5967, pp.812-818, 2010.

[42] M. L. P. Cynthia Rosenzweig, "Potential Impact of Climate Change on World Food Supply," *NATURE* vol. 367, no. 13, 1994.

[43] B. M. Long, B. D. Rae, V. Rolland, B. Forster, and G. D. Price, "Cyanobacterial CO_2-concentrating mechanism components: function and prospects for plant metabolic engineering," *Curr Opin Plant Biol,* vol. 31, pp. 1-8, 2016.

[44] F. Fiorani and U. Schurr, "Future Scenarios for Plant Phenotyping," *Annu Rev Plant Biol,* vol. 64, pp. 267-91, 2013.

[45] Narangerel Altangerel, Gombojav O. Ariunbold, Connor Gorman, Masfer H. Alkahtani, Eli J. Borrego, Dwight Bohlmeyer, Philip Hemmer, Michael V. Kolomiets, Joshua S. Yuan, and Marlan O. Scully, "*In vivo* diagnostics of early abiotic plant stress response via Raman spectroscopy," *Proc Natl Acad Sci U S A,* vol. 114, no. 13, pp. 3393-3396, 2017.

[46] G. R. Cramer, K. Urano, S. Delrot, M. Pezzotti, and K. Shinozaki, "Effects of abiotic stress on plants: a systems biology perspective," *BMC Plant Biol,* vol. 11, p. 163, 2011.

[47] F. Liu, H. Chen, and R. Han, "Different Doses of the Enhanced UV-B Radiation Effects on Wheat Somatic Cell Division," *CellBio,* vol. 04, no. 02, pp. 30-36, 2015.

[48] W. H. Gerhard Ries, Holger Puchta, Heinrich Sandermann, Harald K. Seidlitz Barbara Hohn, "Elevated UV-B radiation reduces genomestability in plants.," *NATURE,* vol. 406, 2000.

[49] P. Pandey, V. Irulappan, M. V. Bagavathiannan, and M. Senthil-Kumar, "Impact of Combined Abiotic and Biotic Stresses on Plant Growth and Avenues for Crop Improvement by Exploiting Physio-Morphological Traits," *Front Plant Sci,* vol. 8, pp. 537, 2017.

[50] P. Shrivastava and R. Kumar, "Soil salinity: A Serious Environmental Issue and Plant Growth Promoting Bacteria as One of the Tools for Its Alleviation," *Saudi J Biol Sci,* vol. 22, no. 2, pp. 123-31, 2015.

[51] A. Skirycz and D. Inze, "More from Less: Plant Growth Under limited Water," *Curr Opin Biotechnol,* vol. 21, no. 2, pp. 197-203, Apr 2010.

[52] D. Tu, W. Zheng, Y. Liu, H. Zhu, and X. Chen, "Luminescent Biodetection Based on Lanthanide-Doped Inorganic Nanoprobes," *Coordination Chemistry Reviews,* vol. 273-274, pp. 13-29, 2014.

[53] E. Pershagen and K. E. Borbas, "Designing Reactivity-Based Responsive Lanthanide Probes for Multicolor Detection in Biological Systems," *Coordination Chemistry Reviews,* vol. 273-274, pp. 30-46, 2014.

[54] Y. Liu, D. Tu, H. Zhu, E. Ma, and X. Chen, "Lanthanide-Doped Luminescent Nano-Bioprobes: from Fundamentals to Biodetection," *Nanoscale,* vol. 5, no. 4, pp. 1369-84, 2013.

[55] L. Qin, X. Meng, J. Zhang, C. Du, L. Zhu, and B. Xu, "Growth and Properties of Nd:$GdVO_4$ Crystal," *Optical Materials,* vol. 23, no. 1-2, pp. 455-459, 2003.

[56] V. Klochkov, N. Kavok, G. Grygorova, O. Sedyh, and Y. Malyukin, "Size and Shape Influence of Luminescent Orthovanadate Nanoparticles on Their Accumulation in Nuclear Compartments of Rat Hepatocytes," *Mater Sci Eng C Mater Biol Appl,* vol. 33, no. 5, pp. 2708-12, 2013.

[57] M. del Barrio *et al.,* "Enzyme-Induced Modulation of the Emission of Upconverting Nanoparticles: Towards a New Sensing Scheme for Glucose," *Biosens Bioelectron,* vol. 59, pp. 14-20, 2014.

[58] A. Hischemöller, J. Nordmann, P. Ptacek, K. Mummenhoff, and M. Haase, "*In-Vivo* Imaging of the Uptake of Upconversion Nanoparticles by Plant Roots," *Journal of Biomedical Nanotechnology,* vol. 5, no. 3, pp. 278-284, 2009.

[59] J. Nordmann, S. Buczka, B. Voss, M. Haase, and K. Mummenhoff, "*In vivo* Analysis of the Size- and Time-Dependent Uptake of NaYF4:Yb,Er Upconversion Nanocrystals by Pumpkin Seedlings," *Journal of Materials Chemistry B,* vol. 3, no. 1, pp. 144-150, 2015.

[60] Yunyun Chen, Carlos Sanchez, Yuan Yue, Mauricio de Almeida, Jorge M. González, Dilworth Y. Parkinson and Hong Liang , "Observation of Yttrium Oxide Nanoparticles in Cabbage (Brassica oleracea) Through Dual Energy K-Edge Subtraction Imaging," *Journal of nanobiotechnology,* vol. 14, no. 1, pp. 23, 2016.

[61] Juanjuan Peng, Yun Sun, Qian Liu, Yang Yang, Jing Zhou, Wei Feng, Xianzhong Zhang, and Fuyou Li, "Upconversion Nanoparticles Dramatically Promote Plant Growth Without Toxicity," *Nano Research,* vol. 5, no. 11, pp. 770-782, 2012.

[62] S. Steinert, F. Ziem, L.T. Hall, A. Zappe, M. Schweikert, N. Go¨tz, A. Aird, G. Balasubramanian, L. Hollenberg and J. Wrachtrup, "Magnetic Spin Imaging Under Ambient Conditions with Sub-Cellular Resolution," *Nat Commun,* vol. 4, pp. 1607, 2013.

[63] R. B. Rodrigues and S. M. Thomaz, "Photosynthetic and Growth Responses of *Egeria Densa* to Photosynthetic Active Radiation," *Aquatic Botany,* vol. 92, no. 4, pp. 281-284, 2010.

[64] S. C. Bustamante Lopez and K. E. Meissner, "Characterization of Carrier Erythrocytes for Biosensing Applications," *J Biomed Opt,* vol. 22, no. 9, pp. 91510, 2017.

[65] C. M. Hu, L. Zhang, S. Aryal, C. Cheung, R. H. Fang, and L. Zhang, "Erythrocyte Membrane-Camouflaged Polymeric Nanoparticles as a Biomimetic Delivery Platform," *Proc Natl Acad Sci U S A,* vol. 108, no. 27, pp. 10980-5, 2011.

[66] S. P. Klinken, "Cells in Focus Red Blood Cells," *The International Journal of Biochemistry & Cell Biology* vol. 34, pp. 1513–1518, 2002.

[67] M. A. M., Sarah C. Ritter, and Kenith E. Meissner, "Encapsulation of FITC to Monitor Extracellular pH: a Step Towards the Development of Red Blood Cells as Circulating Blood Analyte Biosensors," *BIOMEDICAL OPTICS EXPRESS,* vol. 2, no. 7, 2011.

[68] Xi Guo, Yanwen Zhang, Jianbo Liu, Xiaohai Yang, Jin Huang, Li Li, Lan Wan and Kemin Wang "Red Blood Cell Membrane-Mediated Fusion of Hydrophobic Quantum Dots with Living Cell Membranes for Cell Imaging," *Journal of Materials Chemistry B,* vol. 4, no. 23, pp. 4191-4197, 2016.

[69] M. K. Michaela Harz, Stephan St¨ockel, Petra R¨osch, Thomas Deufel and and J. u. Popp, "Analysis of Single Blood Cells for CSF Diagnostics via a Combination of Fluorescence Staining and Micro-Raman Spectroscopy," *Analyst,* vol. 133, pp. 1416–1423, 2008.

[70] Nandan K. Das, Yichuan Dai, Peng Liu, Chuanzhen Hu, Lieshu Tong, Xiaoya Chen and Zachary J. Smith, "Raman Plus X: Biomedical Applications of Multimodal Raman Spectroscopy," *Sensors,* vol. 17, no. 7, 2017.

[71] Zhigang Yang, Amit Sharma, Jing Qi, Xiao Peng, Dong Yeop Lee, Rui Hu, Danying Lin, Junle Qu, Jong Seung Kim, "Super-resolution Fluorescent Materials: An Insight into Design and Bioimaging Applications," *Chemical Society Reviews,* vol. 45, no. 17, pp. 4651-4667, 2016.

[72] D. Williamson, A. Magenau, D. Owen, and K. Gaus, "Biological Fluorescence Nanoscopy," *Understanding Biophotonics: Fundamentals, Advances, and Applications,* pp. 221, 2016.

[73] J. Biteen and K. A. Willets, "Introduction: Super-Resolution and Single-Molecule Imaging,", *Chem. Rev*. vol. 117, pp. 7241−7243, 2017.

[74] A. von Diezmann, Y. Shechtman, and W. Moerner, "Three-Dimensional Localization of Single Molecules for Super-Resolution Imaging and Single-Particle Tracking," *Chemical Reviews* vol. 117, no. 11, pp. 7244-7275, 2017.

[75] S. Saurabh, A. M. Perez, C. J. Comerci, L. Shapiro, and W. Moerner, "Super-Resolution Imaging of Live Bacteria Cells Using a Genetically Directed, Highly Photostable Fluoromodule," *Journal of the American Chemical Society,* vol. 138, no. 33, pp. 10398-10401, 2016.

[76] J . H . Wang , J. D. Ba rtlett , A . C . Dunn , S. Small , S. L. Willis, M. J. Driver and A. L. Lewis , "The Use of Rhodamine 6G and Fluorescence Microscopy in the Evaluation of Ehospholipid-Based Polymeric Biomaterials," *Journal of microscopy,* vol. 217, no. 3, pp. 216-224, 2005.

[77] M. W. Berns, A. E. Siemens, and R. J. Walter, "Mitochondrial Fluorescence Patterns in Rhodamine 6G-Stained Myocardial Cells *in vitro*," *Cell biophysics,* vol. 6, no. 4, pp. 263-277, 1984.

[78] X N He, Y Gao, M Mahjouri-Samani, P N Black, J Allen, M Mitchell, W Xiong, Y S Zhou, L Jiang and Y F Lu, "Surface-Enhanced Raman Spectroscopy Using Gold-Coated Horizontally Aligned Carbon Nanotubes," *Nanotechnology,* vol. 23, no. 20, p. 205702, 2012.

[79] P. Li, X. Zhou, H. Liu, L. Yan, and J. Liu, "Surface-Enhanced Raman Evidence for Rhodamine 6 G and Its Derivative with Different Adsorption Geometry to Colloidal Silver Nanoparticle," *Journal of Raman Spectroscopy,* vol. 44, no. 7, pp. 999-1003, 2013.

[80] A.-I. Henry, B. Sharma, M. F. Cardinal, D. Kurouski, and R. P. Van Duyne, "Surface-Enhanced Raman Spectroscopy Biosensing: *In vivo* Diagnostics and Multimodal Imaging," *Analytical chemistry,* vol. 88, no. 13, pp. 6638-6647, 2016.

[81] K. A. Willets, S. M. Stranahan, and M. L. Weber, "Shedding Light on Surface-Enhanced Raman Scattering Hot Spots Through Single-Molecule Super-Resolution Imaging," *The journal of physical chemistry letters,* vol. 3, no. 10, pp. 1286-1294, 2012.

[82] Katrin Kneipp, Yang Wang, Harald Kneipp, Lev T. Perelman, Irving Itzkan, Ramachandra R. Dasari, and Michael S. Feld "Single Molecule Detection Using Surface-Enhanced Raman Scattering (SERS)," *Physical review letters,* vol. 78, no. 9, pp. 1667, 1997.

[83] Jonas Fölling, Mariano Bossi, Hannes Bock, Rebecca Medda, Christian A. Wurm, Birka Hein, Stefan Jakobs, Christian Eggeling, Stefan W. Hell , "Fluorescence Nanoscopy by Ground-State Depletion and Single-Molecule Return," *Nature methods,* vol. 5, no. 11, pp. 943-945, 2008.

[84] T. Egawa and S.-R. Yeh, "Structural and Functional Properties of Hemoglobins from Unicellular Organisms as Revealed by Resonance Raman Spectroscopy," *Journal of inorganic biochemistry,* vol. 99, no. 1, pp. 72-96, 2005.

[85] D. Rousseau and M. Ondrias, "Resonance Raman Scattering Studies of the Quaternary Structure Transition in Hemoglobin," *Annual review of biophysics and bioengineering,* vol. 12, no. 1, pp. 357-380, 1983.

[86] S. Hoey, D. Brown, A. McConnell, W. Smith, M. Marabani, and R. Sturrock, "Resonance Raman Spectroscopy of Hemoglobin in Intact Cells: A Probe of Oxygen Uptake by Erythrocytes in Rheumatoid Arthritis," *Journal of inorganic biochemistry,* vol. 34, no. 3, pp. 189-199, 1988.

[87] B. R. Wood, P. Caspers, G. J. Puppels, S. Pandiancherri, and D. McNaughton, "Resonance Raman Spectroscopy of Red Blood Cells Using Near-Infrared Laser Excitation," *Analytical and bioanalytical chemistry,* vol. 387, no. 5, pp. 1691-1703, 2007.

[88] R. D. Snook, T. J. Harvey, E. C. Faria, and P. Gardner, "Raman Tweezers and Their Application to the Study of Singly Trapped Eukaryotic Cells," *Integrative Biology,* vol. 1, no. 1, pp. 43-52, 2009.

[89] A. Bankapur, E. Zachariah, S. Chidangil, M. Valiathan, and D. Mathur, "Raman Tweezers Spectroscopy of Live, Single Red and White Blood Cells," *PLoS One,* vol. 5, no. 4, pp. 10427, 2010.

[90] J. L. Deng, Q. Wei, M. H. Zhang, Y. Z. Wang, and Y. Q. Li, "Study of the Effect of Alcohol on Single Human Red Blood Cells Using Near-Infrared Laser Tweezers Raman Spectroscopy," *Journal of Raman Spectroscopy,* vol. 36, no. 3, pp. 257-261, 2005.

[91] C. Eggeling, A. Volkmer, and C. A. Seidel, "Molecular Photobleaching Kinetics of Rhodamine 6G by One- and Two-Photon Induced Confocal Fluorescence Microscopy," *Chemphyschem,* vol. 6, no. 5, pp. 791-804, 2005.

[92] B. R. Wood and D. McNaughton, "Raman Excitation Wavelength Investigation of Single Red Blood Cells *in vivo*," *Journal of Raman Spectroscopy,* vol. 33, no. 7, pp. 517-523, 2002.

[93] G. Rusciano, A. C. De Luca, G. Pesce, and A. Sasso, "Raman Tweezers as a Diagnostic Tool of Hemoglobin-Related Blood Disorders," *Sensors,* vol. 8, no. 12, pp. 7818-7832, 2008.

[94] M. Wahadoszamen, A. Rahaman, N. M. R. Hoque, A. I Talukder, K. M. Abedin, and A. F. M. Y. Haider, "Laser Raman Spectroscopy with Different Excitation Sources

and Extension to Surface Enhanced Raman Spectroscopy," *Journal of Spectroscopy*, vol. 2015, pp. 1-8, 2015.

[95] Lang Rao, Qian-Fang Meng, Lin-Lin Bu, Bo Cai, Qinqin Huang, Zhi-Jun Sun, Wen-Feng Zhang, Andrew Li, Shi-Shang Guo, Wei Liu, Tza-Huei Wang, and Xing-Zhong Zhao "Erythrocyte Membrane-Coated Upconversion Nanoparticles with Minimal Protein Adsorption for Enhanced Tumor Imaging," *ACS Appl Mater Interfaces*, vol. 9, no. 3, pp. 2159-2168, 2017.

[96] C. C. W. Y. Martin, and H. K. Wickramasinghe, "Atomic Force Microscope–Force Mapping and Profiling on a Sub 100-Å scale," *Journal of Applied Physics 61*, vol. 61, no. 4723, 1987.

[97] J. A. Last, P. Russell, P. F. Nealey, and C. J. Murphy, "The Applications of Atomic Force Microscopy to Vision Science," *Invest Ophthalmol Vis Sci*, vol. 51, no. 12, pp. 6083-94, 2010.

[98] G. Binnig, C. F. Quate, and C. Gerber, "Atomic Force Microscope," *Phys Rev Lett*, vol. 56, no. 9, pp. 930-933, 1986.

[99] A. Dzedzickis, V. Bučinskas, N. Šešok, and I. Iljin, "Modelling of Mechanical Structure of Atomic Force Microscope," *Solid State Phenomena*, vol. 251, pp. 77-82, 2016.

[100] P. Johansson, "Geomatry Effects on the Van Der WAlls Force in Atomic Forsce Microscopy.," *PHYSICAL REVIEW B*, vol. 56, no. 7, 1997.

[101] F. LONDO, "The General Theory of Molecular Forces," *physik. Chem*, vol. 11, no. 222, 1936.

[102] J. Manoel, A. Marcelo, A. Madureira, and B. R. d. Pontes Junior, "On an Overview of Nonlinear and Chaotic Behavior and Their Controls of an Atomic Force Microscopy (AFM) Vibrating Problem," in *Nonlinearity, Bifurcation and Chaos - Theory and Applications*, DOI: 10.5772/51834, 2012.

[103] R. A. Murdick, W. Morrison, D. Nowak, T. R. Albrecht, J. Jahng, and S. Park, "Photoinduced Force Microscopy: A Technique for Hyperspectral Nanochemical Mapping," *Japanese Journal of Applied Physics*, vol. 56, no. 8S1, 2017.

[104] W. M. Derek Nowak, H. Kumar Wickramasinghe, Junghoon Jahng, Eric Potma,Lei Wan, and T. R. A. Ricardo Ruiz, Kristin Schmidt, Jane Frommer, Daniel P. Sanders, Sung Park, "Nanoscale Chemical Imaging by Photoinduced Force Microscopy," *Sci. Adv.* , vol. 2, 2016.

[105] F. Huang, V. A. Tamma, Z. Mardy, J. Burdett, and H. K. Wickramasinghe, "Imaging Nanoscale Electromagnetic Near-Field Distributions Using Optical Forces," *Sci Rep,* vol. 5, pp. 10610, 2015.

[106] G. Balasubramanian, A. Lazariev, S. R. Arumugam, and D. W. Duan, "Nitrogen-Vacancy Color Center in Diamond-Emerging Nanoscale Applications in Bioimaging and Biosensing," *Curr Opin Chem Biol,* vol. 20, pp. 69-77, 2014.

[107] J. Jeske *et al.*, "Stimulated Emission from Nitrogen-Vacancy Centres in Diamond," *Nat Commun,* vol. 8, pp. 14000, 2017.

[108] H. J. M. D. Rugar, P. Guergner, S.E. Lambert, J.E. Stern, I. McFadyen, "Magnetic Force Microscopy: General Principles and Application to Longitudinal Recording Media.," *Applied Physics,* vol. 68, no. 3, 1990.

[109] A. I. Melker, V. T. Tung, V. V. Nelayev, S. A. Chizhik, V. V. Chikunov, and T. X. Hoai, "Tapping and Shear-Mode Atomic Force Microscopy Using A Quartz Tuning Fork with High Quality Factor," presented at the Twelfth International Workshop on Nanodesign Technology and Computer Simulations, 2008.

[110] J.-M. F. and É. Carry, "Introduction to The Quartz Tuning Fork," *Am. J. Phys."* , vol. 75, no. 5, 2007.